# Lysosomal proteomics reveals mechanisms of neuronal apoE4-associated lysosomal dysfunction

Einar K. Krogsaeter,[a,b,c,j] Justin McKetney,[a,b,c,j] Angelica Marquez,[a,b,c] Zeynep Cakir,[a,b,c] Erica Stevenson,[a,b,c] Gwendolyn M. Jang,[a,b,c] Antara Rao[d,e], Anton Zhou [d], Yadong Huang,[d,e,f,g,h,i] Nevan J. Krogan,[a,b,c] Danielle L. Swaney[a,b,c,*,#]

[a]Gladstone Data Science and Biotechnology Institute, The J. David Gladstone Institutes, San Francisco, California, USA

[b]Quantitative Bioscience Institute, University of California, San Francisco, California, USA

[c]Department of Cellular and Molecular Pharmacology, University of California, San Francisco, California, USA

[d]Gladstone Institute of Neurological Disease, The J. David Gladstone Institutes, San Francisco, USA

[e]Developmental and Stem Cell Biology Graduate Program, University of California, San Francisco, USA

[f]Neuroscience Graduate Program, University of California, San Francisco, USA

[g]Gladstone Center for Translational Advancement, Gladstone Institutes, San Francisco, USA

[h]Biomedical Sciences Graduate Program, University of California, San Francisco, USA

[i]Departments of Neurology and Pathology, University of California, San Francisco, USA

[j]These authors contributed equally

#Lead contact

*Correspondence: danielle.swaney@ucsf.edu.

## Summary

ApoE4 is the primary risk factor for Alzheimer's Disease. While apoE is primarily expressed by astrocytes, AD pathology including endosomal abnormalities and mitochondrial dysfunction first occurs in neurons.

Lysosomes are poised at the convergence point between these features. We find that apoE4-expressing cells exhibit lysosomal alkalinization, reduced lysosomal proteolysis, and impaired mitophagy. To identify driving factors for this lysosomal dysfunction, we performed quantitative lysosomal proteome profiling. This revealed that apoE4 expression results in lysosomal depletion of Lgals3bp and accumulation of Tmed5 in both Neuro-2a cells and postmitotic human neurons. Modulating the expression of both proteins affected lysosomal function, with Tmed5 knockdown rescuing lysosomal alkalinization in apoE4 cells, and Lgals3bp knockdown causing lysosomal alkalinization and reduced lysosomal density in apoE3 cells. Taken together, our work reveals that apoE4 exerts gain-of-toxicity by alkalinizing the lysosomal lumen, pinpointing lysosomal Tmed5 accumulation and Lgals3bp depletion as apoE4-associated drivers for this phenotype.

**Keywords**: APOE4, Alzheimer's Disease, Lysosomes, pH, Proteomics, Lgals3bp

**Acknowledgements**: This work was supported by National Institutes of Health grants R01AG059751 to NJK and DLS, U54NS123746 to DLS, and R01AG071697 to YH. EKK is a fellow of the California Institute for Regenerative Medicine. Angelica Marquez was supported by the Gladstone Institutes PUMAS program (Promoting Underrepresented Minority Advancement in the Sciences). We thank Robert W. Mahley for helpful discussions. We thank the Gladstone Histology & Light Microscopy Core for supporting all confocal microscopy experiments.

# Introduction

Alzheimer's Disease (AD) is the most common form of dementia and is expected to remain a continuing major global health burden, with cases predicted to double to more than 130 million worldwide by 2050.[1] Although the complexity of AD presents significant challenges for understanding disease progression and developing effective therapeutics, a predominant feature among AD cases is the apolipoprotein (apo) E4 genetic variant.[2,3] This variant is not only found in 60-70% percent of all sporadic and familial AD cases, but is also associated with a lower age of AD onset.[4–6] The apoE4 variant also appears a modifier for autosomal dominant, early-onset AD, accelerating cognitive decline in *PSEN1* E280A carriers.[7] Importantly, carriers of

the APOE4 genotype frequently present with two hallmark pathologies of AD: Tau neurofibrillary tangles (NFTs) and β-amyloid plaques.

Considering that APOE4 is both a strong genetic risk factor for AD and is also relatively common among the general population (20-25%), there have been significant efforts to understand the mechanisms by which APOE4 drives AD biology using both patient samples and diverse model systems. Current evidence indicates that apoE4 expression can be detrimental to a variety of neuronal phenotypes including reduced synaptic plasticity and density,[8–11] reduced hippocampal volume,[12,13] and impaired learning and memory.[14–18] Importantly, these effects can be cell type specific, with evidence for both neuronal[12,19–22] and glial[18,23,24] apoE4 expression individually influencing AD related processes.

At a cellular and molecular level, apoE4 has been implicated with defects in a numerous processes including cytoskeletal and microtubule structure,[25–28] β-amyloid clearance,[29–31] tau dynamics,[12] cellular bioenergetics,[32–34] and endo-lysosomal function.[11,23,35–38] For example, previous observations have shown that apoE4-expressing Neuro-2a cells suffer from metabolic rewiring due to impairments in oxidative phosphorylation and mitochondrial respiration.[34,39,40] These respiratory defects are accompanied by redox imbalance in the form of a shifted $NAD^+$/NADH ratio and excessive generation of radical oxygen species (ROS).[34] Normally, dysfunctional mitochondria would be cleared through mitophagy, allowing new functional mitochondria to replace dysfunctional organelles.[41] The apoE4-associated accumulation of defective mitochondria could suggest underlying impairments in mitophagic flux.

Though various stimuli can induce mitophagy, the processes of mitochondrial clearance converge upon the mitochondrial uptake into acidic lysosomes via autophagic engulfment.[42] Loss of function of lysosomal proteins can result in lysosomal storage and cause AD[43–45] or other similar, early-onset, neurodegenerative diseases.[46–50] Inhibition of lysosomal function also directly leads to development of AD pathological features such as β-amyloid accumulation.[51–53] Importantly, apoE4 expression is also associated with altered endosomal trafficking and accumulation of protein aggregates that would normally be degraded by lysosomes, including β-amyloid.[54] Beyond APOE, mutations within other genetic risk factors for AD, such

as rare presenilin-1 (PSEN1) mutations are associated with early-onset AD, cause lysosomal mislocalization of the γ-secretase complex, resulting in an intracellular pool of aggregation-prone Aβ42.[55]

While PSEN1 is known to directly regulate lysosomal acidification and function,[56] the effect of apoE4 on lysosomal homeostasis remains incompletely explored. A recent article described how exogenously administered apoE4 preferentially traffics to late endosomes/lysosomes and impairs autophagic flux.[57] Furthermore, astrocytic apoE4 expression results in excessive endosomal acidification. Intriguingly, these authors also found apoE4 astrocytes to exhibit lysosomal alkalinization, without exploring the molecular mechanisms regulating this process or the further ramifications of this on cellular function.[23] Accordingly, we hypothesized that apoE4 expression may intrinsically influence lysosomal function in neurons, the cell type most impacted by AD. To investigate this, we have used both neuron-like cell models (Neuro-2a) and human iPSC-derived neurons to evaluate how apoE4 expression results in lysosomal dysfunction, and identified alterations to lysosomal proteins that drive this phenotype.

# Results

## *ApoE4-associated lysosomal dysfunction impairs mitochondrial clearance*

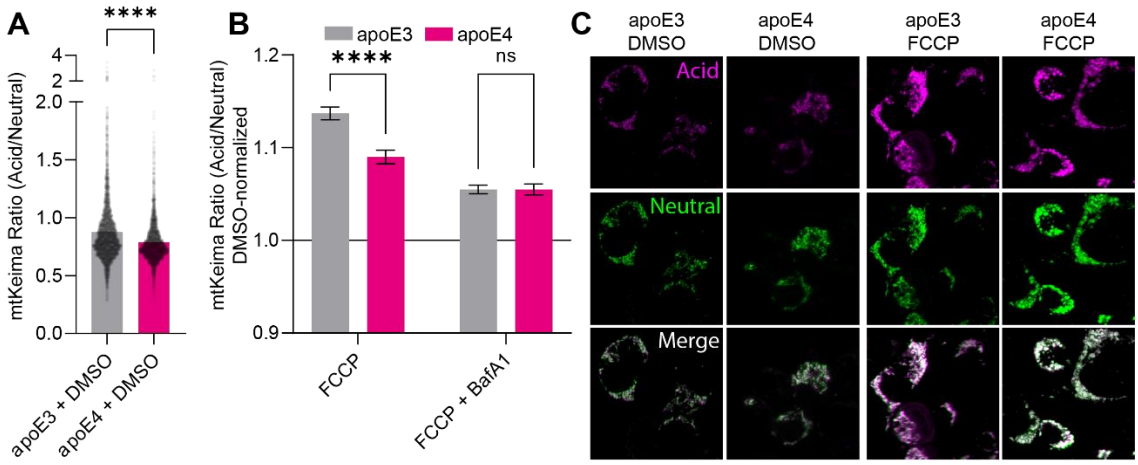


**Figure 1: Mitophagy is impaired in apoE4-expressing cells**. (**A**) mtKeima was used to target the Keima pH sensor to mitochondria in apoE3 and apoE4-expressing cells. (**B**) Neuro-2a cells expressing mtKeima were subjected to 1 hour treatment with the mitochondrial uncoupling agent FCCP or co-treatment with

FCCP and BafA1 to inhibit lysosomal acidification. (**C**) Representative images for (A-B). Experiments were performed as three technical and biological replicates. The mtKeima ratio was calculated in Fiji by dividing the intensity of the acid label by the neutral label for individual mitochondria. The data was plotted as means with SEM error bars, and analyzed in GraphPad Prism by unpaired, two-tailed t-test (A) or 2-way ANOVA followed *post-hoc* by Bonferroni's multiple comparisons test (B).

Since apoE4-expressing cells appear to accumulate dysfunctional mitochondria, we hypothesized that mitochondrial clearance mechanisms might be defective. While various stimuli can induce mitophagy, the processes of mitochondrial clearance converge upon the mitochondrial uptake into acidic lysosomes via autophagic engulfment.[42] Accordingly, mitophagy can be readily measured using the mtKeima probe, consisting of the pH-sensitive fluorophore Keima fused to the COX VIII mitochondrial targeting sequence. We transfected Neuro-2a cells stably expressing either apoE3 or apoE4 with mtKeima to monitor mitophagy either under basal conditions, or upon inducing mitophagy by adding the mitochondrial uncoupler FCCP. Under basal conditions, there was a modest impairment of mitophagy in apoE4 cells, with apoE4 mitochondria residing in more alkaline environments than their apoE3 counterparts (Fig. 1A). While FCCP-induced mitochondrial depolarization triggered mitophagy in both apoE3- and apoE4-expressing cells, the mitochondrial uptake into acidic environments appeared stronger in the apoE3-expressing cells, even when correcting for the already higher baseline (Fig. 1B-C). To validate that the mtKeima probe was in fact detecting the uptake of mitochondria into lysosomes, we combined the FCCP treatment with bafilomycin A1 (BafA1). BafA1 is a potent inhibitor of the lysosomal $H^+$ pump, blocking lysosomal acidification. Accordingly, we detected a reduction in the acidic mtKeima signal by its application (Fig. 1B). Intriguingly, BafA1 treatment abrogated the difference between apoE3- and apoE4-expressing cells, suggesting that differences in lysosomal acidification could underlie the observed mitophagic defects.

## *ApoE4 expression dramatically abrogates lysosomal function*

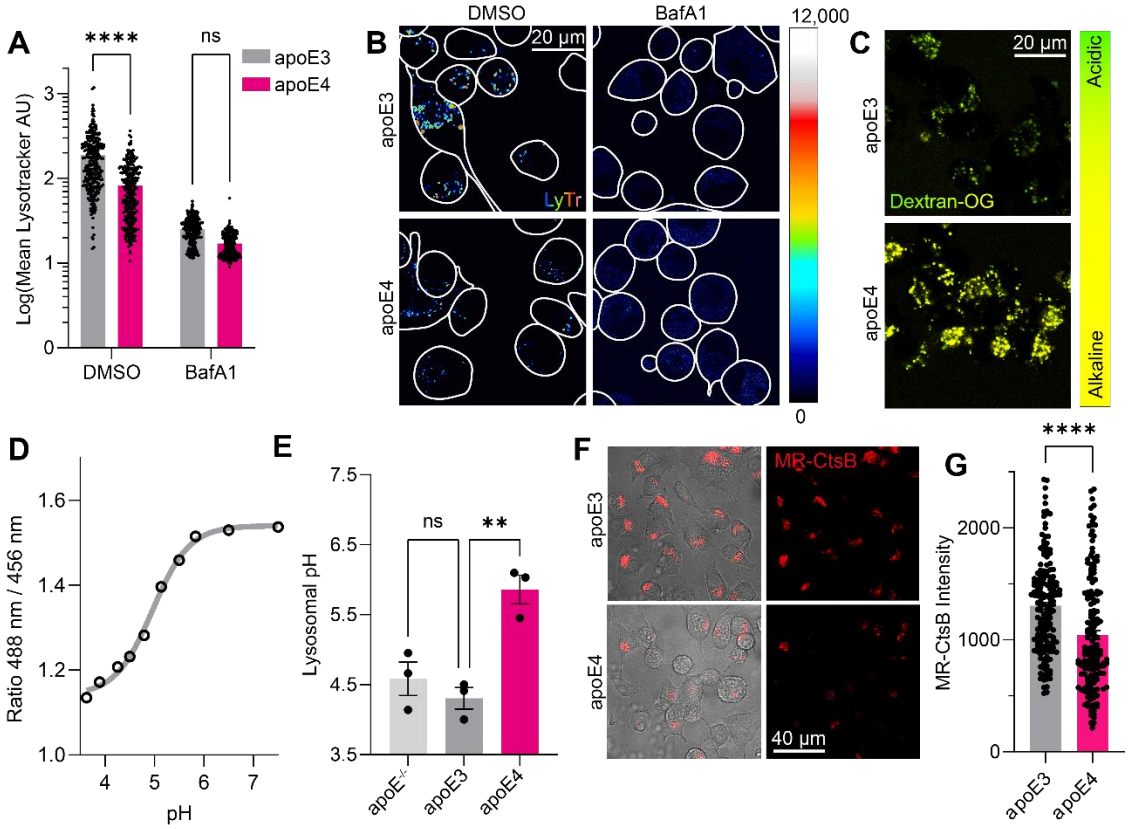


**Figure 2: ApoE4 expression impairs lysosomal function**. (**A**) LysoTracker Deep Red was used to stain acidic compartments for 30 minutes before confocal imaging, and the staining intensity calculated for each cell. Bafilomycin A1 was administered to block lysosomal acidification, decreasing the lysotracker staining intensity. (**B**) Representative images for (A). (**C**) Quantification of lysosomal pH using OregonGreen-70,000 kDa Dextran. (**D**) Generation of a standard curve for the OregonGreen ratio by pH-clamping and imaging of the cells, and (**E**) extrapolation of lysosomal pH values. (**F**) Interrogation of lysosomal cathepsin-dependent activity by the fluorogenic probe MagicRed Cathepsin B (MR-CtsB). (**G**) Quantification of (F), showing decreased cathepsin proteolysis in apoE4-expressing cells. Experiments were performed as three technical and biological replicates. The Lysotracker, OregonGreen, and MR-CtsB intensities were calculated in Fiji for each labelled cell. The data was analyzed in GraphPad Prism by 2-way ANOVA followed *post-hoc* by Bonferroni's multiple comparisons test (A), one-way ANOVA followed *post-hoc* by Bonferroni's multiple comparisons test (E), or by unpaired, two-tailed t-test (G).

In the light of the observed mitophagic defects, we continued to investigate lysosomal function in the apoE4-expressing Neuro-2a cells. While it has previously been shown that apoE4 expression alkalinizes the lysosomal pH of mouse astrocytes,[23] the effects of apoE4 expression on lysosomal function in neuronal cells, as well as the consequences of lysosomal alkalinization, remain incompletely characterized. To assess whether apoE4 expression influences lysosomal acidification, we stained apoE3- and apoE4-expressing cells with the acidotropic dye Lysotracker. The intensity of Lysotracker staining correlates with the expanse of the endolysosomal system and/or the endolysosomal pH, where a higher staining intensity corresponds with more acidic structures in the cells. The Lysotracker staining intensity was significantly reduced in apoE4-expressing cells (Fig. 2A-B), suggesting either endolysosomal alkalinization or a reduction in endolysosomal structures. Upon immunostaining for the lysosomal membrane marker LAMP1, we found the lysosomal density to, if anything, be higher in apoE4-expressing cells (Suppl. Fig. 1A-B).

Next, to accurately measure the lysosomal pH, we employed the OregonGreen probe. Similarly to mtKeima, OregonGreen allows ratiometric pH measurements. OregonGreen can be targeted to lysosomes through conjugation to Dextran, loading overnight, and chasing for 60 minutes to allow its efflux from endosomal (but not lysosomal) compartments. Following initial measurements, we pH-clamped the lysosomes using a range of standard buffers to generate a standard curve of OregonGreen intensities (Fig. 2D). By doing so, we could extrapolate the OregonGreen intensity ratios to absolute pH values. We found the apoE4-expressing cells to exhibit dramatic lysosomal alkalinization (pH=5.86) compared to apoE3 (pH=4.30) and apoE$^{-/-}$ (pH=4.58) cells (Fig. 2C-E), reminiscent of previous work in apoE4-expressing astrocyte lysosomes (pH=5.20, compared to pH=4.08 in apoE3-expressing controls).[23] Of note, apoE3 expression did not significantly alter the lysosomal pH compared to apoE$^{-/-}$ cells (Fig. 2E), suggesting that apoE4 expression may confer a toxic gain-of-function to Neuro-2a lysosomes. The lysosomal pH gradient is tightly coupled to lysosomal calcium storage through $H^+/Ca^{2+}$ antiporters.[58] Similarly, increased levels of luminal cations aside from protons can drive lysosomal alkalinization by polarizing the membrane potential. To measure whether the lysosomal pH changes are accompanied by luminal $Ca^{2+}$ changes in apoE4 cells, we targeted a previously described[59] genetically encoded calcium indicator to the lysosomes to measure lysosomal calcium release. Using GPN to release lysosomal calcium,[60] we found lysosomal calcium levels to be comparable between

apoE3 and apoE4-expressing cells (Suppl. Fig. 1C-H), particularly after correcting for lysosomal density (Suppl. Fig. 1I). These findings suggest that the apoE4-associated lysosomal alkalinization is distinct from lysosomal $Ca^{2+}$ storage.

Lysosomes normally maintain their pH at a range between 4.00 and 5.00 to support their resident, $H^{+}$-dependent proteases (such as the cathepsins). Lysosomal alkalinization occurs upon ageing and cellular senescence, resulting in impaired lysosomal proteolysis and accumulation of protein aggregates. Hypothesizing that the apoE4-associated lysosomal alkalinization also impairs lysosomal degradation, we loaded the cells with Magic Red Cathepsin B (MR-CtsB), a dye that is endocytosed, transported to lysosomes, and becomes fluorescent upon its proteolytic cleavage. We found that the apoE4-expressing cells exhibited decreased MR-CtsB proteolysis compared to apoE3-expressing cells, in line with their decreased lysosomal acidity (Fig. 2F-G). Having established that neuronal apoE4 expression leads to lysosomal impairment, we set out to explore the mechanisms underlying this phenomenon.

155 ***Identification of lysosomal proteins via LysoIP proteomics***

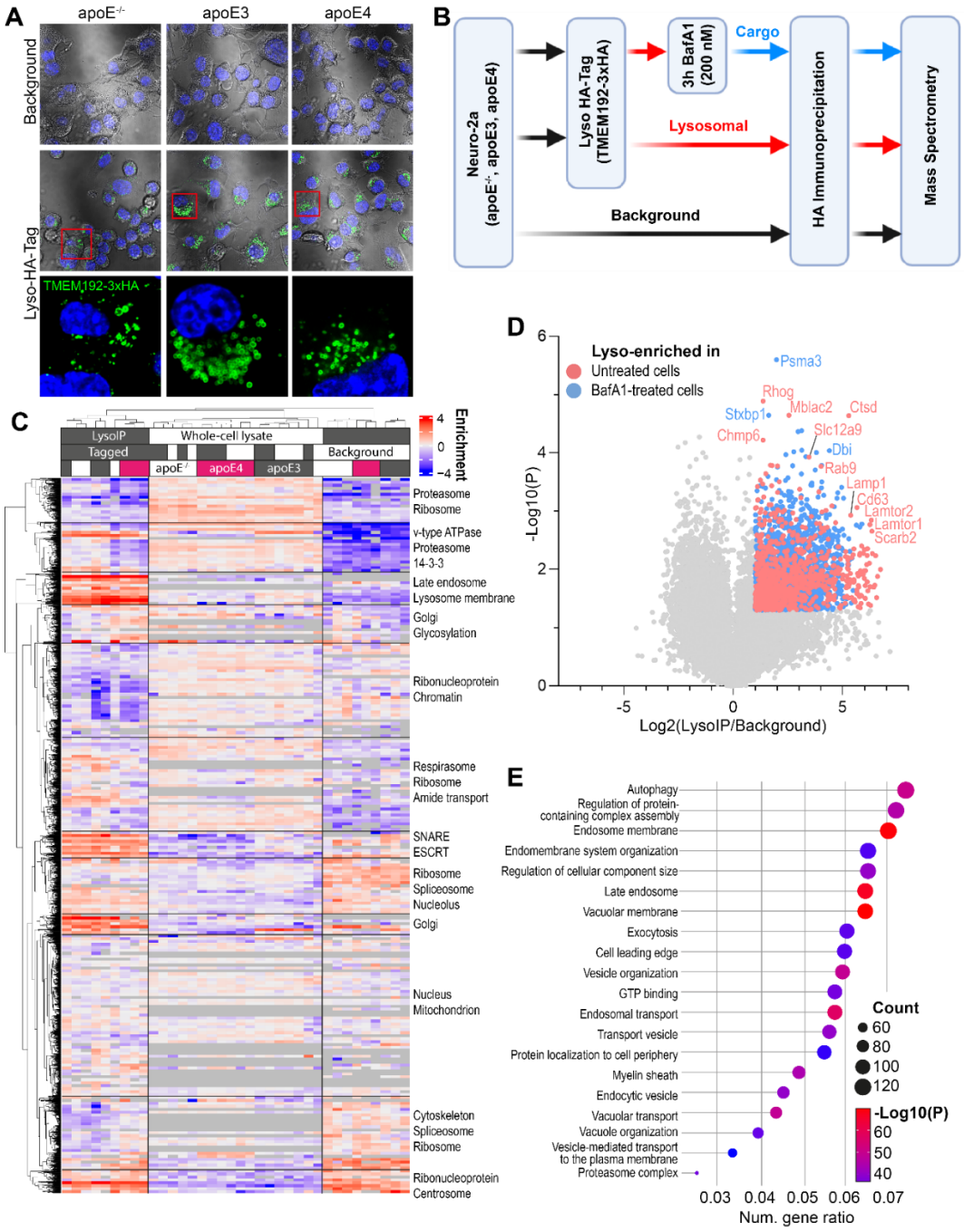


**Figure 3: Isolation of lysosomes by lysosomal immunoprecipitation (LysoIP).** (**A**) Immunostaining of the lysosomal TMEM192-3xHA tag shows immunoreactivity only in transduced cells. (**B**) Schematic of the LysoIP workflow. Note, paired samples from whole cell lysates of each of these conditions were also analyzed. (**C**) Clustered heat map of protein abundances. Only those proteins with a protein abundance

signal intensity exceeding $2^{14}$ in LysoIP experiments are included, which represent approximately the 80% most abundant proteins per genotype. (**D**) Lysosomal proteins were defined based on enrichment relative to background samples. (**E**) Enriched gene ontology terms in LysoIP samples reveal lysosome-associated functions.

Since proteins serve as the principal biological effectors that are likely the most intrinsically tied to the observed lysosomal impairment, we opted to assess changes to the lysosomal proteome upon apoE4 expression. Accordingly, we transduced and stably selected apoE$^{-/-}$, apoE3-expressing, and apoE4-expressing Neuro-2a cells with lentiviruses encoding the lysosomal tag TMEM192-3xHA.[61] Lysosomes were visualized in transduced cells by immunostaining for the 3xHA tag, with no immunoreactivity in background cells (Fig. 3A). We performed immunoprecipitation of the tagged lysosomes (LysoIP) to isolate lysosomes and assess the lysosomal proteome, using cells lacking the TMEM192-3xHA tag as a background proteome to control for non-specific binding to the anti-HA beads (Fig. 3B). Additionally, to provide greater context for alterations observed in the lysosomal proteome, we also measured protein abundances from un-enriched whole cell lysates for each of the apoE genotypes. As expected, clustering of protein abundances across all samples revealed distinct proteome signatures between the three different experimental groups (whole cell lysate, LysoIP, and background), with further subclusters primarily driven by the apoE allele (Fig. 3C).

Next, we focused on defining the lysosomal proteome. First, we identified enriched lysosomal proteins by comparing the tagged and background samples for each genotype. We considered proteins to be lysosomal if they were either exclusively detected in LysoIP samples, or significantly enriched in LysoIP samples relative to background samples (>2-fold, and $p<0.05$) (Fig. 3D). Gene ontology analysis of the identified lysosomal proteins revealed enrichment of terms associated with lysosomal function, such as autophagy, endosome membrane, late endosome, and vacuolar membrane (Fig. 3E). As expected, the most significantly enriched proteins included well-known lysosomal proteins widely appreciated for their role in facilitating lysosomal function, including degradative enzymes (Ctsd, Psma3), proton pump subunits (Atp6v1e1), metabolic enzymes (Gusb), and lysosomal scaffold proteins (Lamtor 2/4). However, we also found a number of proteins to be detected exclusively and reproducibly across all lysosomal samples, but that have not yet been ascribed a lysosomal function. These include constituents of the Usp8:Ptpn23:Stam2 and

Nedd4:Litaf:Bmpr1 deubiquitin- and ubiquitination complexes, and the early endosome/Rab5a-associated proteins Rabep1 and Rabgef1 (Suppl. Fig. 2B). While neither complex is appreciated to function in the lysosome, their respective implicated processes of protein ubiquitination and Rab protein activation could conceivably be of lysosomal importance. Lastly, the primary driver of differences between LysoIP samples, as determined by principal component analysis (PCA), was found to be bafilomycin treatment, (Suppl. Fig. 4A), and was distinguished by lysosomal accumulation of chaperonin TCP-1 subunits, proteasome subunits, and recruitment of the dynein complex, alongside loss of several lysosomal proteins including cathepsins, the GATOR2 complex, and glycosyl hydrolases.

## *Proteomic alterations to apoE4-associated lysosomes*

After demonstrating successful enrichment of lysosomal proteins, we next focused on investigating the consequences of apoE4 expression on the lysosomal proteome, particularly in light of the lysosomal disturbances observed in apoE4-expressing cells. While nearly identical protein populations were detected in lysosomes across all genotypes (Suppl. Fig. 2C), their relative abundances were distinct. Accordingly, lysosomal proteomes could be separated by genotype both by principal component analysis (PCA; Fig. 4A) and hierarchical clustering (Suppl. Fig. 3 and 3A; Fig. 3B). PCA component 2 (11.6% variance) separated apoE3- and apoE4-expressing samples based on apoE4-associated accumulation of glucosyl hydrolases, Lamtor proteins, and a number of Golgi-associated vesicle proteins, while enzymes regulating aminoacyl-tRNA biosynthesis and gluconeogenesis were absent. Component 3 (7.4% variance) separated apoE$^{-/-}$ lysosomes from apoE-expressing lysosomes, marked by apoE-dependent accumulation of sterol transporters and proton pump subunits, and a depletion of proteasome subunits and microtubule proteins (Fig. 4A). Comparing apoE4- to apoE3-expressing cells, we observed an increase in the ER-to-Golgi-transporting TMEDs (Suppl. Fig. 4B), which have previously been implicated in sorting misfolded proteins to the lysosomes.[62] The proton-pump-coupled anion exchanger Slc26a11[63] and zinc transporter Slc36a11 were also found at higher levels in apoE4 lysosomes (Suppl. Fig. 4B). Intriguingly, most lysosomal proteins with lower abundance in apoE4 cells were in fact Bafilomycin A1-sensitive proteins that accumulate upon proton pump blockade, including the phospho-Tau-binding protein Scrn1 (Suppl. Fig. 4B).[64] The few intrinsically lysosomal proteins expressed at lower levels in apoE4 lysosomes include the ADP ribosylation factor

activator Arfgef3/Big3 regulating lysosomal trafficking,[65] and the glycoprotein Lgals3bp/90K-BP/Mac-2BP (Fig. 4B, Suppl. Fig. 4B).

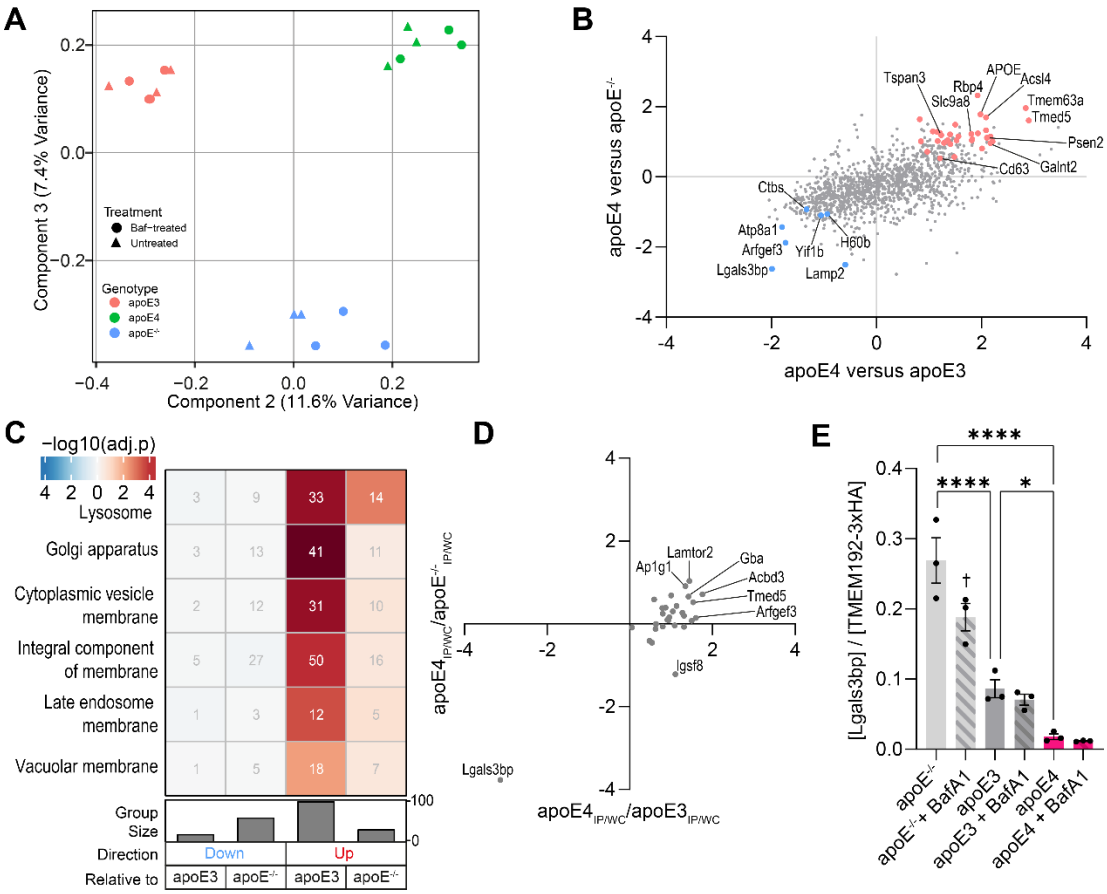


**Figure 4: The apoE4-associated lysosomal proteome.** (**A**) PCA separates lysosomes by genotype. (**B**) Correlation of apoE4-associated lysosomal protein changes relative to both controls. Axes are geometric means of Log2(apoE4/control) and -Log10(P) values. Colored proteins were statistically significantly depleted (blue) or accumulated (red) in apoE4 lysosomes. (**C**) GO terms associated with apoE4-associated proteins. (**D**) Over- and underrepresented lysosomal proteins relative to their respective whole-cell levels, as described in the Methods section. (**E**) The lysosomal Lgals3bp level depends on apoE expression and proton pump activity.

Since the apoE4 allele is thought to confer a neuronal gain-of-toxicity effect that would not be observed in apoE-deficient or apoE3-expressing cells,[21,66,67] we extended our comparisons of the lysosomal proteome to

apoE$^{-/-}$ cells to identify lysosomal proteins differentially regulated uniquely in apoE4 cells. We considered proteins significant if they changed in the same direction and reached statistical significance relative to both apoE$^{-/-}$ and apoE3 controls. We found that apoE4-expressing lysosomes uniquely accumulated Bafilomycin A1-insensitive proteins, including APOE itself, the early onset familial AD-associated secretase subunit Psen2, the secretase-modulating Cd63 and Tspan3, the trafficking adaptors Ap1s1, Ap1g1, Bet1l, Lamtor1, Lamtor2, and Tmed5, the lipid/glycan-associated Acsl4, Acbd3, Galnt2, Man2b1, Neu1, Pip4p1, Sacm1l, Tmem55b, Uxs1, the mechanosensitive cation channel Tmem63a/Osca, and the transporters Abcb6 (porphyrins), Slc9a8/NHE8 ($H^+$-coupled sodium), Slc36a1 ($H^+$-coupled amino acids), Slc39a11 (zinc), and Spns1 (lysosphingolipids) (Fig. 4B, Suppl. Fig. 4B-C). The proteins accumulating in apoE4 lysosomes were principally enriched in the "Lysosome" gene ontology (GO) term, even when correcting for the already lysosome-laden background proteome (Fig. 4C, Suppl. Fig. 4D). Proteins annotated under the Golgi apparatus, particularly chaperones and proteins ensuring its structural integrity, also accumulated in apoE4 lysosomes (Fig. 4C). Fewer changes were observed in the opposite direction, with the apoE4-expressing lysosomes expressing lower levels of the aforementioned Arfgef3 and Lgals3bp, alongside the phospholipid flippase Atp8a1, the lysosomal autophagy regulator Lamp2, the glycoprotein-degrading Ctbs, the ER-Golgi trafficking regulator Yif1b, and the Klrk1 ligand H60b (Fig. 4B, Suppl. Fig. 4B-C). Conversely, downregulated cargo proteins particularly included proteins involved in tRNA synthesis (Suppl. Fig. 4D).

Since changes in the lysosomal proteome could be secondary to whole-cell protein level changes, we correlated the expression level of dysregulated lysosomal proteins to their whole cell levels. As expected, we observed a robust correlation between apoE4-associated lysosomal protein level changes and changes to the whole-cell protein level (Suppl. Fig. 4E). We hypothesized that proteins that were over- or underrepresented on apoE4 lysosomes could reflect changes in their lysosomal uptake and/or clearance. For example, a lysosome-accumulating protein that decreases on the whole-cell level could reflect its increased trafficking to the lysosome, resulting in lysosomal degradation. Conversely, a protein depleted from lysosomes but accumulating in the whole cell could suggest impaired lysosomal uptake, and result in its cellular accumulation. To investigate such possibilities, we plotted lysosomal under- or overrepresented proteins in the context of the apoE4 genotype. Note, proteins not detected in whole-cell samples could not be plotted,

precluding similar analyses of 15 proteins including Psen2 and Rbp4. This approach highlighted the unique case of Lgals3bp, a protein unchanged in the whole-cell level while its expression was dramatically reduced in apoE4-expressing lysosomes (Fig. 4D). In contrast, several proteins were overrepresented in the lysosome, including Lamtor2, Ap1g1, Acbd3, and Tmed5, although these changes appeared less striking. Performing a partial least squares discriminant analysis to identify proteins characteristically separating lysosomes of one genotype from others further highlighted Lgals3bp depletion to be a characteristic feature of apoE4-expressing lysosomes (Suppl. Fig. 4F). Intriguingly, lysosomal Lgals3bp levels appeared sensitive to both apoE and proton pump blockade, with apoE$^{-/-}$ lysosomes boasting the highest Lgals3bp levels and apoE4 + BafA1 lysosomes containing the least Lgals3bp (Fig. 4E). This approach thereby revealed a set of apoE4-dysregulated lysosomal proteins where lysosomal protein abundance changes were not indirectly driven by changes in whole cell expression, but rather directly driven by changes to how these proteins are recruited to and cleared from the lysosome.

Having observed a number of proteomic alterations to the apoE4 lysosomes, we assessed whether similar proteomic changes occur in lysosomes of human, postmitotic neurons. We used isogenic apoE3/apoE4 iPSCs to differentiate neurons that have previously been used to study apoE4-associated neurodegeneration.[21] We generated iPSC-differentiated neuronal progenitors using small molecules for 3 weeks, followed by terminal differentiation and maturation for another 4 weeks to obtain a mixed neuronal culture including GABAergic interneurons (Suppl. Fig. 5A). We next profiled changes in lysosomal LGALS3BP and TMED5 levels using a proximity ligation assay (PLA) as described in Figure 5A. Proximity ligation assays are typically used to profile protein-protein interactions, yielding fluorescent signals when the donor and acceptor proteins are within 40 nm of each other.[68] However, the lysosomal lumen is a compact and protein-dense compartment, with a radius ranging from 100-300 nm.[69,70] We therefore hypothesized that coincidental interactions between LAMP1 and our proteins of interest would occur more frequently in the lysosomal lumen, and thereby be picked up by proximity ligation. We first established our proximity ligation assays. The LAMP1-LAMP1 positive control yielded a particularly good signal-to-noise ratio over the single-antibody controls, whereas the LAMP1-LGALS3BP and LAMP1-TMED5 yielded comparatively less efficient, yet still significant, lysosomal PLA signals (Suppl. Fig. 5B-C). Having established that we could detect lysosomal LGALS3BP

and TMED5, we compared lysosomal PLA signals between apoE3 and apoE4 neurons. In concordance with our observations in Neuro-2a cells, we found apoE4 iPSC-derived neuronal lysosomes to contain significantly less LGALS3BP and significantly more TMED5 than their apoE3 counterparts (Fig. 5B-C). These results illustrate that the apoE4-associated lysosomal protein changes observed extend beyond Neuro-2a cells, and also manifest in human postmitotic neurons susceptible to neurodegeneration.

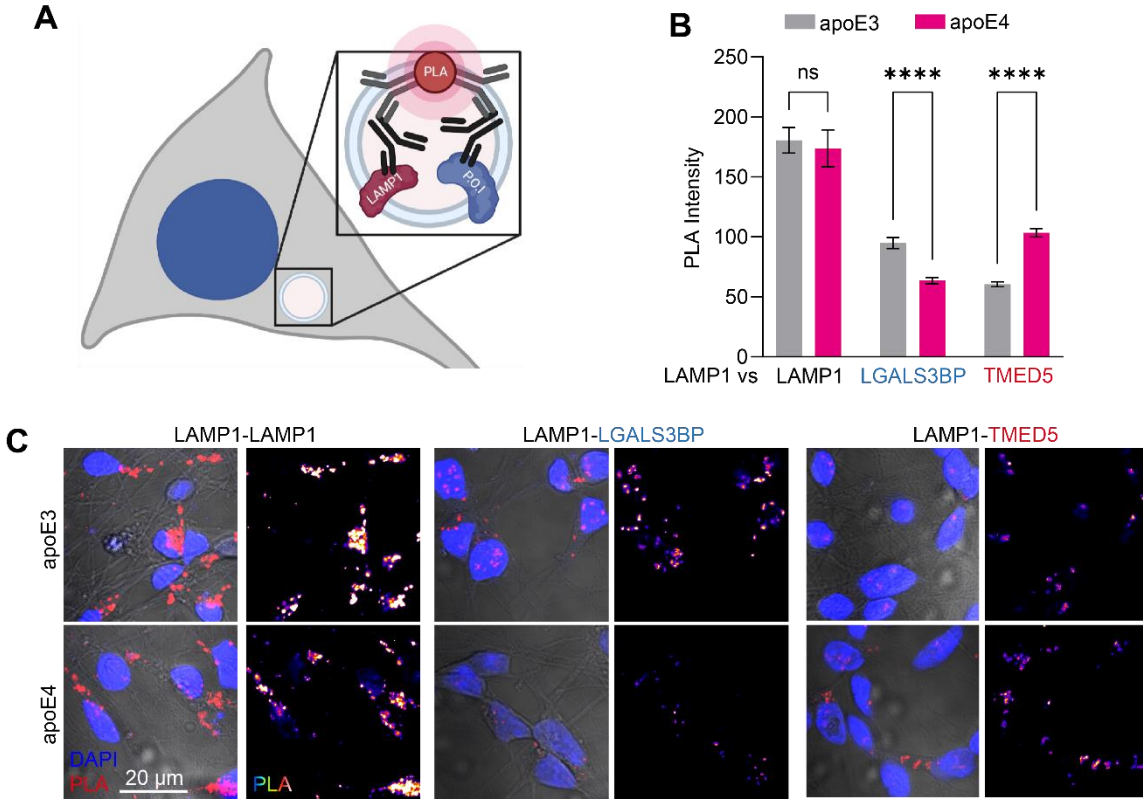


**Figure 5: ApoE4-associated lysosomal protein changes in iPSC-derived neurons.** (**A**) Schematic of lysosomal proximity ligation assay, whereby proximity ligation occurs between luminal lysosomal LAMP1 and the profiled protein of interest (P.O.I). (**B**) Results from proximity ligation assay. LAMP1-LAMP1 proximity ligation was used as a positive control, and lysosomal LGALS3BP and TMED5 localization profiled by proximity ligation against LAMP1. apoE4 lysosomes showed significant LGALS3BP depletion and TMED5 accumulation relative to apoE3 controls. (**C**) Representative images.

### *Neuronal apoE4 expression modulates the Lgals3bp interactome*

While the biology surrounding proteins such as Tmed5 and the function of its associated Tmed protein family is comparatively well-explored, Lgals3bp is not part of a wider protein family. Instead, it has primarily been explored in the context of centriolar function and its extracellular secretion.[71–74] Structurally, Lgals3bp consists of three domains – An N-terminal Scavenger Receptor Cysteine-Rich (SRCR) domain associated with phagocytosis of negatively charged ligands including lipoproteins,[75] a BTB domain that recruits ubiquitin ligase complexes, and a BTB- and Kelch-associated BACK domain, whose function remains speculative (Suppl. Fig. 6).[76] This domain architecture suggests that Lgals3bp could function as a scaffold for SRCR substrates and ubiquitin ligases associated with the BTB-BACK domain, facilitating substrate ubiquitination and degradation. While a recent proteomics screen highlighted Lgals3bp as a lysosomal protein in several cell-lines,[77] the lysosomal function of Lgals3bp is largely unknown. Thus, to interrogate the mechanistic importance of differential lysosomal Lgals3bp localization in the context of apoE4 expression, we assessed the cellular localization and protein-protein interactome of Lgals3bp. We transiently transfected apoE3- and apoE4-expressing Neuro-2a cells with Lgals3bp-GFP, and evaluated its distribution across cellular compartments. We found that only a minor fraction of overexpressed Lgals3bp-GFP colocalized with lysosomes and mitochondria, while most Lgals3bp localized to the endoplasmic reticulum (Suppl. Fig. 7A-C). Indeed, our findings are in line with subcellular fractionation data, showing Lgals3bp to be predominantly retrieved from ER, lysosomal lumen, and mitochondrial intermembrane space fractions, while minor Lgals3bp populations associate with membrane- and nucleus-associated fractions.[78] These results are also in agreement with our proteomics findings, wherein the total cellular levels of Lgals3bp were unchanged between apoE3 and apoE4 cells, despite large differences at the lysosome, suggesting that the lysosomal Lgals3bp fraction represents a minor population of this protein within the cell.

Next, we evaluated the Lgals3bp interactome by affinity-purification mass spectrometry (APMS). We transiently transfected apoE3- and apoE4-expressing Neuro-2a cells with either Lgals3bp-GFP or GFP for 3 days. Cells were harvested, affinity-enriched for GFP, and interacting proteins eluted for mass spectrometric analysis as previously described.[28] Within a respective apoE genotype cell line, proteins found to be consistently detected in all Lgals3bp-GFP replicates and significantly enriched over GFP-transfected controls

were considered Lgals3bp interaction partners. The obtained datasets could be readily clustered based on the overexpressed protein, indicating a distinct Lgals3bp-GFP interactome not governed by its GFP affinity tag (Suppl. Fig. 7D). Having identified Lgals3bp interactors, we used STRING[79] to annotate protein complexes within the Lgals3bp interaction network (Suppl. Fig. 7E). Lgals3bp-associated proteins and protein complexes were ordered into subcellular compartments (Fig. 6). While previously studies have focused on its functions as a secretory[72–74] or centriole-associated protein[71], Lgals3bp is associated with a diversity of protein complexes. These include nuclear interactors such as the U2/U5 spliceosomes, a host of Hnrn proteins and other proteins shuttling between the cytosol and nucleus, the outer nuclear pore complex NUP107-160, and nuclear import factors. The endoplasmic reticulum (ER)-associated Lgals3bp-interacting protein complexes include the 80S ribosome, ER folding machinery and chaperones, proteins regulating the ER-associated degradation (ERAD) pathway, and cargo-transporting proteins associated with the ER-Golgi intermediate compartment (ERGIC). We also identified a number of interacting mitochondrial protein complexes regulating transmembrane transport, including three Vdac proteins, a number of proteins in the citric acid cycle, and particularly complex 1, 2, and 4 of the electron transport chain. Cytoplasmic interactors include cytoskeletal actins, tubulins, and effectors, Hsc70 complex subunits implicated in chaperone-mediated autophagy (CMA), and lysosomal proteins regulating membrane trafficking and lysosomal acidification (notably Atp6v1a/h).

Since the apoE4-associated Lgals3bp lysosomal depletion could be caused by a changed Lgals3bp interactome, we assessed how apoE4 expression affected the Lgals3bp interactome. Normalizing the Lgals3bp interactor levels to the measured Lgals3bp levels, we compared Lgals3bp interactor levels between apoE3- and apoE4-expressing Neuro-2a cells. The apoE4 allele context significantly increased Lgals3bp interaction with the ER-associated Acsl4 (not detected in apoE3 cells), Tmed10, and Rpl12, the nuclear Mcm3, Ran and Sec13, the mitochondrial Immt and the cytosolic Ywhag (Fig. 6; Suppl. Fig. 7F). Conversely, the apoE4 allele context decreased the interaction of Lgals3bp with several proteins, including the nuclear Kpnb1 (not detected in apoE4 cells) and Myef2, the ER-associated P4ha1 and the ERAD-associated Faf2, the cytosolic Srm, and the mitochondrial Ogdh, Tufm, and ATP synthase subunits (Fig. 6; Suppl. Fig. 7F). While some altered interactions were associated with overall decreased protein expression (particularly the

mitochondria-associated proteins), altered interactions with nuclear Myef2, Kpnb1, mitochondrial Immt, Rpl12, and Ywhag could not be explained by decreased protein expression levels, suggesting a more direct influence of apoE4 on these Lgals3bp interactions (Suppl. Fig. 7G). These findings show that apoE4 modulates expression of Lgals3bp interaction partners to regulate its subcellular localization, including the nuclear import/export machinery and the secretory receptor Tmed10. In the context of decreased lysosomal Lgals3bp uptake, the decreased interaction between Lgals3bp and the ERAD-targeting Faf2 stands out as a road block for routing Lgals3bp from the ER towards the lysosome.

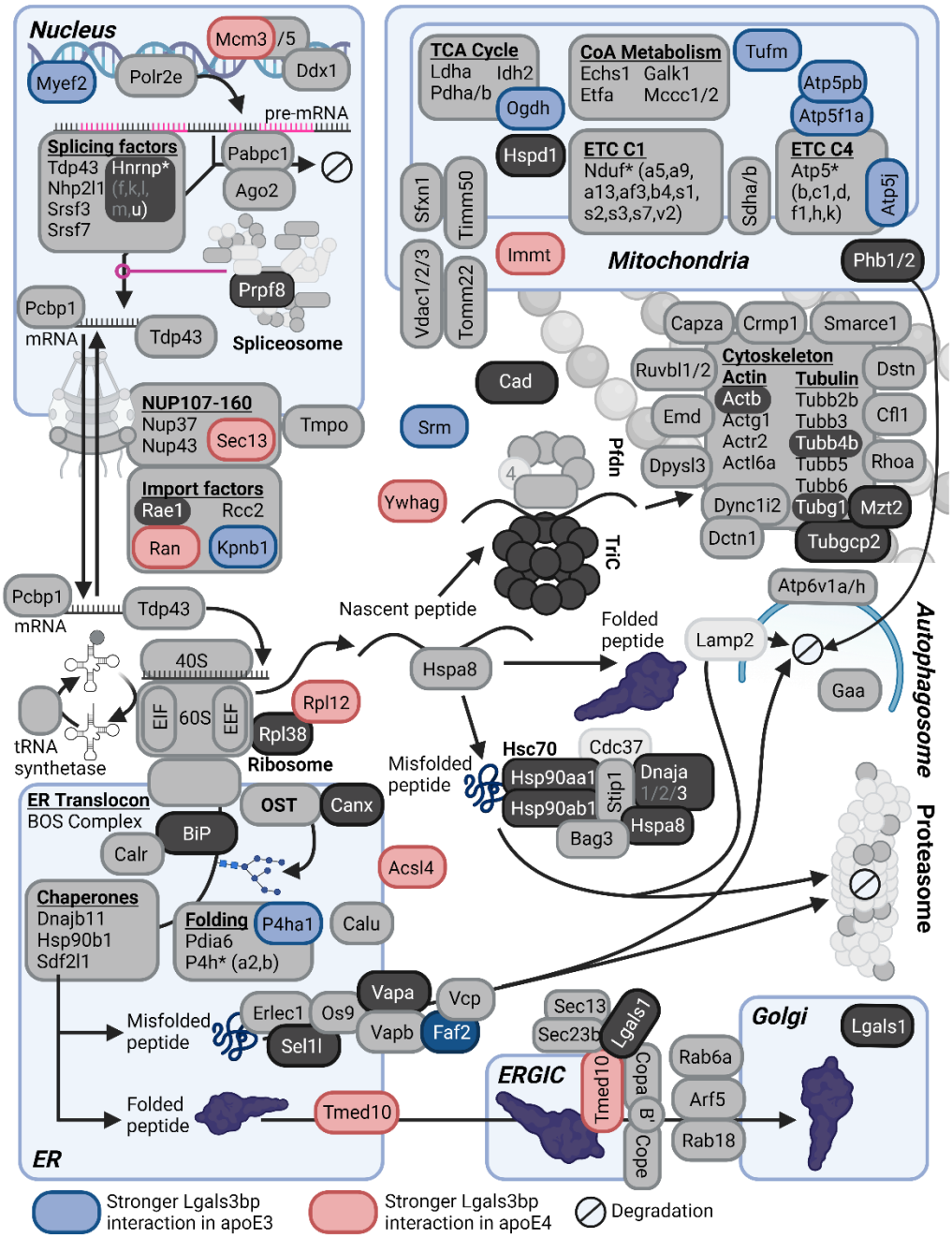


**Figure 6: The apoE-sensitive Lgals3bp interactome.** Proteins found to specifically bind Lgals3bp-GFP are highlighted and situated in their canonical cellular compartment. White nodes indicate proteins in Lgals3bp-associated pathways or complexes that were not pulled down; association with grey proteins were unchanged by apoE genotype; colored protein nodes indicate preferential association with Lgals3bp in the context of apoE3 (blue) or apoE4 (red) genotypes. Interaction nodes with white font and darker

coloring have also been previously described, as reported in the BioGRID protein interaction repository.[80] The illustration was created with BioRender.com.

## *ApoE4-associated drivers of lysosomal dysfunction*

Having identified lysosomal proteins that are specifically sensitive to apoE4-expression, we next assessed whether genetic knockdown of these proteins affect lysosomal acidification. Specifically, we targeted Lgals3bp as the only downregulated protein in apoE4 lysosomes, being the primary characteristic protein separating apoE4 lysosomes from apoE$^{-/-}$ and apoE3 lysosomes. We also targeted APOE, which accumulated in apoE4 lysosomes and constitutes the direct difference between apoE$^{-/-}$, apoE3-, and apoE4-expressing cells. App also accumulated in apoE4 lysosomes, and was particularly intriguing as its cleavage product β-amyloid has been implicated in AD pathogenesis and lysosomal permeabilization in apoE4 contexts.[81] Furthermore, since the apoE4-accumulating protein Psen2 is similarly implicated in amyloidogenic cleavage, we targeted the late endosomal/lysosomal γ-secretase subunit.[55] The chaperone for misfolded GPI-anchored proteins, Tmed5, was one of the most significantly accumulating proteins relative to both apoE$^{-/-}$ and apoE3 controls, and was thus also targeted due to its accumulation in apoE4-associated lysosomes. Finally, we also targeted the AD-associated tau protein (i.e. *Mapt*), which has been previously shown to be disrupted in apoE4-expressing neuronal cells.[12,21,82,83] While we did not consistently detect tau in lysosomes by mass spectrometry, it has recently been reported to spread through lysosomes[84,85], and could be speculated to also influence lysosomal function. As expected, we found S202/T205-phosphorylated tau to be present within lysosomes of iPSC-derived human neurons, albeit at very low levels (Suppl. Fig. 8; Suppl. Video S1). Nonetheless, these findings support previous notions of tau interfacing with the autophagic/lysosomal system[84–92], highlighting that a minor fraction of hyperphosphorylated tau could directly affect lysosomal function.

We first confirmed that our siRNAs downregulated their target transcripts by RT-qPCR (Fig. 7A), before evaluating their influence on lysosomal acidification. We considered a protein a hit if knockdown resulted in a reversal of the apoE4-associated phenotype. Specifically, we found knockdown of the apoE4-accumulating

Tmed5 and the AD-associated tau to increase the LysoTracker staining in both apoE3 and apoE4 cells (Fig. 7B-C). It thereby appears that tau accumulation leads to lysosomal defects, and that its silencing enhances lysosomal function. Conversely, we found Lgals3bp knockdown to result in decreased lysotracker staining in apoE3-expressing cells, mimicking the apoE4 phenotype (Fig. 7B-C). We further confirmed by Oregon-green relative pH measurement that Lgals3bp knockdown moderately impaired lysosomal acidification in apoE3-expressing cells, while significantly reducing the lysosomal density (Fig. 7D,F). Conversely, we silenced Tmed5 in apoE4 cells, which our LysoIP experiments revealed to accumulate in apoE4 lysosomes. Tmed5 knockdown did not affect the lysosomal density, but significantly acidified apoE4 lysosomes (Fig. 7E-F). Taken together, we have identified proteomic driving forces for apoE4-associated lysosomal dysfunction: Fulfilling hypothesis 1, Tmed5 accumulates in apoE4 lysosomes, with its knockdown restoring lysosomal acidity. Fulfilling hypothesis 2, Lgals3bp is depleted from apoE4 lysosomes, and its silencing in apoE3-expressing cells leads to lysosomal alkalinization and decreases the lysosomal density (Fig. 7G). Changes to these lysosomal proteins thereby connect apoE4 expression with the observed lysosomal impairments (Fig. 7H).

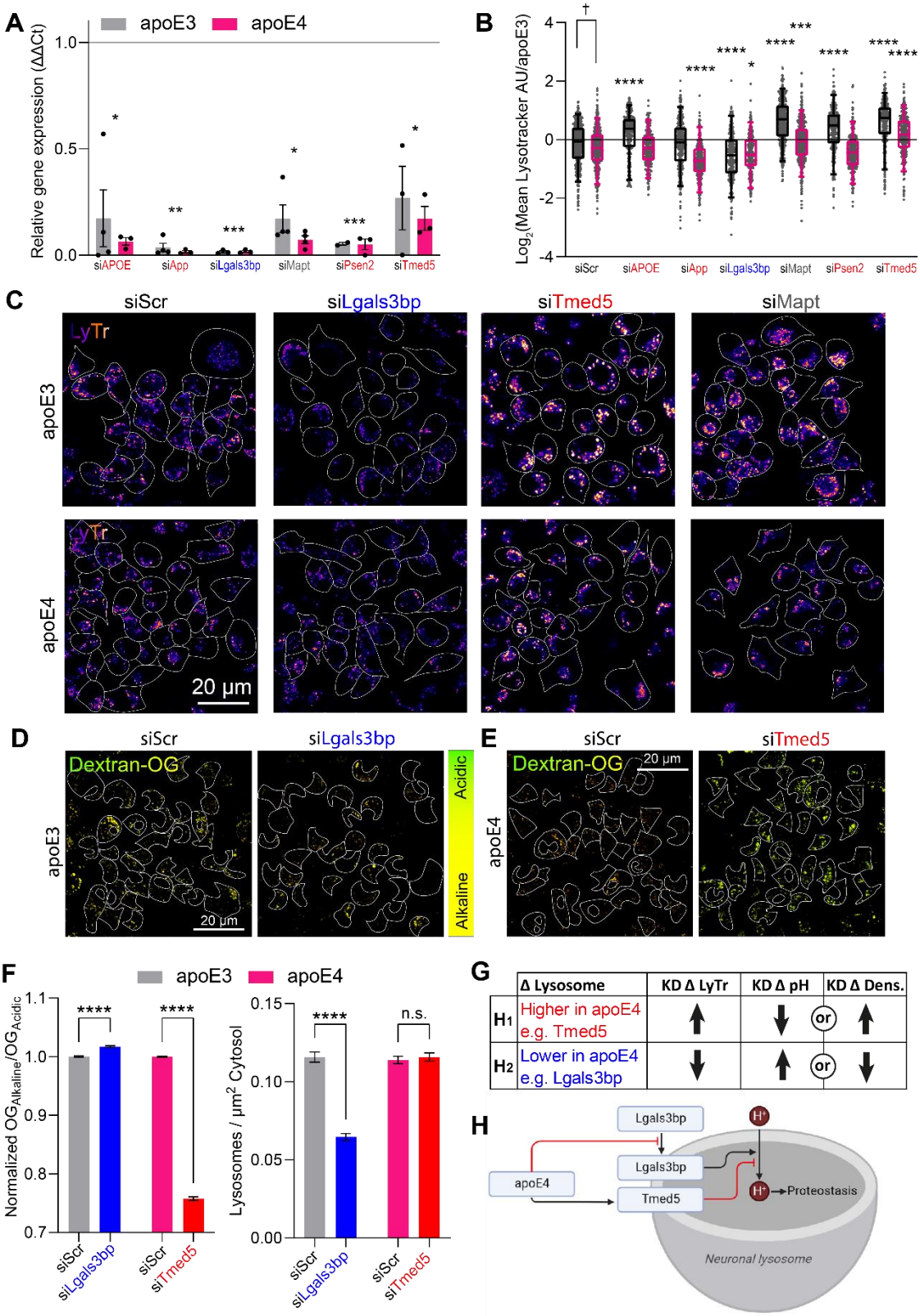
A
apoE3
apoE4
Relative gene expression (ΔΔCt)
siAPOE
siApp
siLgals3bp
siMapt
siPsen2
siTmed5
B
Log2(Mean Lysotracker AU/apoE3)
siScr
siAPOE
siApp
siLgals3bp
siMapt
siPsen2
siTmed5
C
siScr
siLgals3bp
siTmed5
siMapt
apoE3
apoE4
LyTr
20 µm
D
siScr
siLgals3bp
Dextran-OG
Acidic
Alkaline
20 µm
E
siScr
siTmed5
Dextran-OG
20 µm
F
apoE3
apoE4
Normalized OGAlkaline/OGAcidic
Lysosomes / µm2 Cytosol
n.s.
siScr
siLgals3bp
siTmed5
G
Δ Lysosome
KD Δ LyTr
KD Δ pH
KD Δ Dens.
H1
Higher in apoE4
e.g. Tmed5
or
H2
Lower in apoE4
e.g. Lgals3bp
H
Lgals3bp
apoE4
Tmed5
Proteostasis
Neuronal lysosome

**Figure 7: ApoE4-associated proteomic drivers of lysosomal impairment.** (**A**) Expression of target genes following 48 hr knockdown, relative to scrambled controls (siScr). (**B**) Quantification of LysoTracker staining of acidic compartments. Gene names are colored according to their apoE4-associated lysosomal accumulation (red) or depletion (blue). (**C**) Representative LysoTracker images of positive hits. (**D**) Oregon-green relative pH measurement upon knockdown of Lgals3bp in apoE3 cells as compared to scrambled controls. (**E**) Oregon-green relative pH measurement upon knockdown of Tmed5 in apoE4 cells. (**F**) Quantification of Oregon Green measurements from panels D-E, showing relative pH and lysosomal density. (**G**) Graphical representation of hypotheses. (**H**) Graphical representation of experimental results. All experiments were performed as three technical and biological replicates. Fluorophore intensities and spot counting was performed in Fiji. Data was analyzed in GraphPad Prism by one-sampled t-test against a hypothetical value of 1 (A, B†), or by 2-way ANOVA followed *post-hoc* by Dunnett's multiple comparisons test (B, G).

# Discussion

Regardless of its etiology, Alzheimer's Disease is riddled with signs of impaired lysosomal function: In healthy neurons, lysosomes would normally clear β-amyloid[93,94] and phospho-Tau aggregates,[95] alongside dysfunctional organelles.[96] In the AD brain however, neuronal dysfunction of lysosomes drives the accumulation of AD-associated protein aggregates.[97] We find that neuronal expression of apoE4, the primary genetic risk factor for AD, impairs lysosomal function. It is established that astrocytes which express high apoE4 levels suffer from lysosomal alkalinization by unknown mechanisms.[98] While neuronal cells express less apoE4 than astrocytes, we observe a substantial degree of lysosomal alkalinization, which impairs both lysosomal proteolysis and mitophagy.

Focusing on the classical AD hallmark proteins App (forming toxic β-amyloid and β-CTF) and Mapt/tau (forming neurofibrillary tangles), we found apoE4 lysosomes to accumulate App and contain hyperphosphorylated tau. While silencing *App* or its associated γ-secretase *Psen2* had no effect on lysosomal function in apoE4-expressing cells, tau removal significantly improved lysosomal function. These findings highlight a discordance between how the two classical AD aggregates affect cellular function, and reveal a

vicious cycle between tau and lysosomes: While lysosomal dysfunction on one hand results in tau accumulation[84,86,88,89,91], we find that tau accumulation itself impairs lysosomal activity. This vicious cycle becomes particularly intriguing in the context of apoE4-associated lysosomal impairment. One could expect that in the absence of other insults, removal of either apoE4 or tau prevents the observed, self-perpetuating lysosomal impairment culminating in neurodegeneration. Indeed, this has been previously alluded to, as removal of endogenous tau prevents apoE4-associated neurodegeneration,[99] and neuronal *APOE4* removal from a tauopathy mouse model prevents tau pathology and associated neurodegenerative phenotypes.[12] The convergence of apoE4 and tau on the lysosomal system warrants further investigation, particularly in the context of ongoing clinical trials targeting tau or lysosomes to treat AD.[100]

We explored proteomic alterations to apoE4 lysosomes using LysoIP, finding apoE4 lysosomes to carry higher levels of lysosome- and Golgi-associated proteins. In line with previous studies,[57,101] we found apoE4 to preferentially localize in lysosomes relative to its apoE3 counterpart. This has been postulated as a route for apoE4 to escape the secretory pathway, allowing its membrane interaction, cytosolic entry, and subsequent interference with intracellular processes.

Intriguingly, apoE4 expression causes lysosomal accumulation of several Golgi-associated Transmembrane emp24 domain-containing (Tmed) proteins, including Tmed3, Tmed4, Tmed5, and Tmed9. A number of Tmed proteins are dysregulated in mild cognitive impairment (MCI) or AD brains: While TMED5 expression increases in the AD parietal cortex,[102] expression of both TMED4 and TMED9 decreases in the AD frontal cortex.[103–105] Tmed proteins regulate processing of secretory proteins, and have been primarily studied in the context of coatomer (COP) cargo selection and vesicle formation. However, Tmed proteins also have roles in later secretory compartments.[106] In particular, Tmed5 and Tmed9 have been implicated in trafficking misfolded GPI-anchored proteins from the plasma membrane to the lysosome, alongside Tmed2 and Tmed10.[62] In line with our own findings, knockdown of TMED2 and TMED10 in human iPSC-derived neurons result in increased lysotracker staining,[107] highlighting that coupling of TMED expression and lysosomal function is conserved across species.

There is growing evidence that Lgals3bp may have diverse functional roles. Lgals3bp has been studied in the context of cancer biology, and more recently, its neurological involvement has been described in the process of neurodevelopmental corticogenesis. In concordance to our findings in apoE4 lysosomes, Lgals3bp expression appears decreased post-in mortem in the Alzheimer's Disease entorhinal cortex.[108] While its lysosomal function remains uncharacterized, recent proteomics experiments have demonstrated this protein to be consistently recovered from lysosomes across cell lines.[77] Our results support these previous findings of Lgals3bp as a lysosomal protein, and provide insights into how it affects lysosomal function. As Lgals3bp has been localized to extracellular vesicles that form in late endosomal or lysosomal compartments[109] and suppresses endosomal β-amyloid production,[110] it is conceivable that Lgals3bp facilitates multivesicular body formation, lipid sequestration, and fine-tunes β-amyloid generation to prevent β-amyloid-mediated lysosomal damage. We furthermore find Lgals3bp to interact with several subunits of the ER-associated degradation (ERAD) machinery, which routes misfolded proteins for degradation. We show that apoE4 impairs the interaction between Lgals3bp and the E3 ubiquitin ligase-adaptor Faf2/Ubxd8,[111] plausibly decreasing its lysosomal uptake. Upon genetically decreasing Lgals3bp expression in apoE3 cells, we find that sufficient Lgals3bp protein levels are important for maintaining lysosomal density, and to a lesser extent to maintain lysosomal acidity.

Importantly, while we find that while lysosomal Lgals3bp and Tmed5 are both differentially regulated by apoE4 expression, their impact on lysosomal function is not limited to the context of apoE4. Instead, increased Lgals3bp and decreased Tmed5 may be characteristic of lysosomal health and capable of regulating lysosomal function. This is exemplified by targeted Lgals3bp knockdown resulting in decreased lysosomal density and acidification in apoE3-expressing cells, and CRISPRi-mediated knockdown of several TMED-proteins increasing lysotracker staining in wild-type iPSC-derived neurons.[107] Taken together, our results points at novel mediators of lysosomal pH homeostasis, and highlight their functional relevance in a disease context. Since lysosomal pH dysregulation occurs in a number of diseases beyond Alzheimer's Disease including Parkinson's Disease, lupus, infectious diseases, cancers, and diabetes, a better understanding of the processes underlying these phenomena bears promise of broad translational impact.[112]

## Author Contributions

**Conceptualization:** EKK, ZC, DLS. **Data curation:** JM. **Formal analysis:** EKK, JM, AM. **Funding acquisition:** YH, NJK, DLS. **Investigation:** EKK, JM, AM, ES, GMJ, AR, AZ. **Methodology:** EKK, JM, GMJ, AR, AZ, YH, DLS. **Project administration:** DLS. **Resources:** YH, NJK, DLS. **Software:** JM. **Supervision**: EKK, YH, NJK, DLS. **Validation:** EKK, JM. **Visualization:** EKK, JM. **Writing – original draft:** EKK, DLS. **Writing – review & editing:** EKK, JM, GMJ, YH, NJK, DLS.

## Declaration of Interests

Yadong Huang is a co-founder and scientific advisory board member of GABAeron. The Krogan Laboratory has received research support from Vir Biotechnology, F. Hoffmann-La Roche, and Rezo Therapeutics. Nevan J. Krogan has previously held financially compensated consulting agreements with the Icahn School of Medicine at Mount Sinai, New York, and Twist Bioscience Corp. He currently has financially compensated consulting agreements with Maze Therapeutics, Interline Therapeutics, Rezo Therapeutics, and GEn1E Lifesciences, Inc. He is on the Board of Directors of Rezo Therapeutics and is a shareholder in Tenaya Therapeutics, Maze Therapeutics, Rezo Therapeutics, and Interline Therapeutics. Danielle L. Swaney has financially compensated consulting agreements with Maze Therapeutics and Rezo Therapeutics. The other authors declare no competing interests.

## STAR Methods

### *Key Resources Table*

| REAGENT or RESOURCE | SOURCE | IDENTIFIER |
|---|---|---|
| Antibodies | | |
| anti-HA, mouse monoclonal | BioLegend | #901501 |
| anti-GABA, rabbit polyclonal | Thermo Fisher | #PA5-32241 |
| anti-Lamp1, rat monoclonal | Santa Cruz | #sc-19992 |
| anti-LAMP1, mouse monoclonal | Santa Cruz | #sc20011 |
| anti-LAMP1, rabbit monoclonal | Cell Signaling Technologies | #9091S |
| anti-LGALS3BP, rabbit polyclonal | Thermo Fisher | #10281-1-AP |
| anti-Phospho-Tau-Ser202/Thr205, rabbit polyclonal | ABclonal | #AP0894 |
| anti-TMED5, rabbit polyclonal | Thermo Fisher | #PA5-141055 |
| anti-TuJ, mouse monoclonal | Promega | #G712A |
| anti-Mouse IgG, goat polyclonal, Alexa488-conjugated | Thermo Fisher | #A11001 |
| anti-Rabbit IgG, donkey polyclonal, Alexa488-conjugated | Thermo Fisher | #A21206 |

| | | |
|---|---|---|
| anti-Rat IgG, rabbit polyclonal, Fluorescein-conjugated | Vector | #FI-4000 |
| anti-Mouse IgG, donkey polyclonal, Alexa555-conjugated | Thermo Fisher | #A31570 |
| anti-Rabbit IgG, goat polyclonal, Alexa555-conjugated | Thermo Fisher | #A21428 |
| anti-HA magnetic beads | Thermo Fisher | #88837 |
| anti-GFP Trap beads | Chromotek | #GTMA-10 |
| Chemicals, peptides, and recombinant proteins | | |
| MEM, GlutaMAX™ Supplement | Thermo Fisher | #41090-036 |
| Fetal Bovine Serum | Thermo Fisher | #A31605-02 |
| Non-Essential Amino Acids | Thermo Fisher | #11140050 |
| Sodium Pyruvate | Thermo Fisher | #11360070 |
| Accutase | Fisher Scientific | #NC9839010 |
| Lipofectamine 2000 | Thermo Fisher | #11668019 |
| OptiMEM Reduced Serum Medium | Thermo Fisher | #31985062 |
| Lipofectamine RNAi Max | Thermo Fisher | #13778150 |
| Poly-L-Lysine Solution | Sigma Aldrich | #P4707 |
| Phosphate-Buffered Saline | Corning | #21-030-CV |
| Paraformaldehyde | Sigma Aldrich | #F8775 |
| Hoechst 33342 | Thermo Fisher | #H3570 |
| CytoSeal™ 60 | VWR | #8310-4 |
| Lysotracker Red DND-99 | Thermo Fisher | #L7528 |
| CellMask™ Deep Red Plasma Membrane Stain | Thermo Fisher | #C10046 |
| OregonGreen™, Dextran 70,000 MW | Thermo Fisher | #D7172 |
| Dimethyl Sulfoxide | Sigma Aldrich | #D2650 |
| Bafilomycin A1 | Fisher Scientific | #AAJ61835MCR |
| Gly-Phe-β-naphthylamide | Cayman | #14634 |
| Ionomycin | Cayman | #10004974 |
| Carbonyl cyanide 4-(trifluoromethoxy)phenylhydrazone (FCCP) | Sigma Aldrich | #SML2959 |
| Penicillin-Streptomycin | Corning | #30-002-CI |
| DMEM, 4.5 g/L glucose, L-glutamine | Corning | #10-017-CV |
| PolyJet In Vitro DNA Transfection Reagent | SignaGen | #SL100688 |
| Polybrene | Millipore | #TR-1003-G |
| Puromycin | Thermo Fisher | #A1113802 |
| Matrigel | Corning | #354277 |
| mTESR Plus Media | StemCell Technologies | #100-0274 |
| Y-27632 ROCK inhibitor | Tocris | #1254 |
| DMEM, 4.5 g/L glucose, GlutaMAX | Thermo Fisher | #10-566-024 |
| KnockOut Serum Replacement | Thermo Fisher | #10828028 |
| SB-431542 | Stemgent | #04-0010-10 |
| LDN-193189 | Stemgent | #04-0074 |
| InSolution Wnt Agonist IWP2 | Millipore | #506072 |
| InSolution Smoothened Agonist SAG | Millipore | #566661 |
| FGF8 | Peprotech | #100-25 |
| Laminin, natural mouse protein | Thermo Fisher | #23017-015 |
| DMEM/F12 | Thermo Fisher | #11330-032 |
| N2 Supplement | Thermo Fisher | #17502-048 |

| | | |
|---|---|---|
| Neurobasal | Thermo Fisher | #21103-049 |
| B27 Supplement | Thermo Fisher | #17504-044 |
| BDNF | Peprotech | #450-02 |
| GDNF | Peprotech | #450-10 |
| Critical commercial assays | | |
| NEBuilder HiFi DNA Assembly Master Mix | New England Biolabs | #E2621L |
| RNeasy Mini Kit | Qiagen | #74106 |
| Superscript IV Kit | Thermo Fisher | #18090010 |
| Power SYBR Green PCR Master Mix | Thermo Fisher | #4367659 |
| TaqMan™ Fast Advanced Master Mix for qPCR | Thermo Fisher | #4444963 |
| Intracellular pH Calibration Buffer Kit | Thermo Fisher | #P35379 |
| Duolink® In Situ Red Starter Kit Mouse/Rabbit | Millipore | #DUO92101 |
| Deposited data | | |
| Proteomic raw and processed data | This Paper | PRIDE ProteomeXchange Consortium: PXD044942; Tables S2-S3 |
| Experimental models: Cell lines | | |
| Neuro-2a neuroblastoma cells | Harris *et al*., 2004[82] | N/A |
| Neuro-2a neuroblastoma cells, apoE3-humanized | Harris *et al*., 2004[82] | N/A |
| Neuro-2a neuroblastoma cells, apoE4-humanized | Harris *et al*., 2004[82] | N/A |
| Neuro-2a neuroblastoma cells, TMEM192-3xHA tag | This paper | N/A |
| Neuro-2a neuroblastoma cells, apoE3-humanized, TMEM192-3xHA tag | This paper | N/A |
| Neuro-2a neuroblastoma cells, apoE4-humanized, TMEM192-3xHA tag | This paper | N/A |
| Skin-derived human iPSCs, isogenic apoE3/apoE3 | Wang *et al*., 2018[21] | N/A |
| Skin-derived human iPSCs, isogenic apoE4/apoE4 | Wang *et al*., 2018[21] | N/A |
| Oligonucleotides | | |
| Lgals3bp forward primer, insert into pEGFP-N3: caagcttcgaattcagggacATGGCTCTCCTGTGGCTC | This paper | N/A |
| Lgals3bp reverse primer, insert into pEGFP-N3: cctgtggagccggtggagccCACCATGTCAGTGGAGTTAG | This paper | N/A |
| pEGFP-N3 forward primer: GGCTCCACCGGCTCCACA | This paper | N/A |
| pEGFP-N3 reverse primer: GTCCCTGAATTCGAAGCTTGAGCTC | This paper | N/A |
| qPCR assay: *App* | Thermo Fisher | #Mm01344172_m1 |
| qPCR assay: *Hprt* | Thermo Fisher | #Mm01545399_m1 |
| qPCR assay: *Lgals3bp* | Thermo Fisher | #Mm00478303_m1 |
| qPCR assay: *Mapt* | Thermo Fisher | #Mm00521988_m1 |
| qPCR assay: *Psen2* | Thermo Fisher | #Mm00448405_m1 |
| qPCR assay: *Tmed5* | Thermo Fisher | #Mm00547008_m1 |
| siRNA: *APOE* | Thermo Fisher | #AM16708_41598 |
| siRNA: *App* | Thermo Fisher | #s62516 |
| siRNA: *Lgals3bp* | Thermo Fisher | #AM16708_162469 |
| siRNA: *Mapt* | Thermo Fisher | #s70123 |
| siRNA: *Psen2* | Thermo Fisher | #AM16708_68876 |
| siRNA: Scramble control | Thermo Fisher | #4390844 |
| siRNA: *Tmed5* | Thermo Fisher | #AM16703_83238 |

| | | |
|---|---|---|
| Recombinant DNA | | |
| Plasmid: LAMP2-GCaMP6s | Li *et al*., 2019[59] | Addgene #154151 |
| Plasmid: pΔ-NRF Gag-Pol-Tat-Rev | Bouhaddou *et al*., 2020[113] | pJH-045 |
| Plasmid: pMD2.G VSV-G | Bouhaddou *et al*., 2020[113] | pJH-046 |
| Plasmid: pLJC5-TMEM192-3xHA | Abu-Remaileh *et al*., 2017[61] | Addgene #102930 |
| Plasmid: pCAGGS mitoKeima | Li *et al*., 2021[114] | N/A |
| Plasmid: Lgals3bp-GFP | This paper | N/A |
| Plasmid: LAMP1-mGFP | Falcon-Perez *et al*., 2005[115] | Addgene #34831 |
| Software and algorithms | | |
| ClueGO | Bindea *et al*., 2009[116] | https://apps.cytoscape.org/apps/cluego |
| Cytoscape | Shannon *et al*., 2003[117] | https://cytoscape.org |
| ImageJ/Fiji | Schindelin *et al*., 2012[118] | https://imagej.net |
| MaxQuant | Cox and Mann, 2008[119] | https://www.maxquant.org |
| RStudio | RStudio: Integrated Development for R. RStudio | http://www.rstudio.com |
| Other | | |
| Micro Slides | VWR | #48311-307 |
| ibiTreat ibidi 8-well Live-cell Imaging Chambers | ibidi | #80806 |

## *Resource Availability*

### Lead Contact

Further information and requests for resources and reagents should be directed to and will be fulfilled by the lead contact, Danielle L. Swaney (danielle.swaney@ucsf.edu).

### Materials Availability

All unique and stable reagents, including plasmids and Lyso-IP cell lines generated in this study, are available from the lead contact without restriction.

### Data and Code Availability

The dataset supporting the conclusions of this article is available in the ProteomeXchange Consortium (http://proteomecentral.proteomexchange.org) via the PRIDE partner repository with dataset identifier PXD044942, and can be accessed using the following credentials: Username: reviewer_pxd044942@ebi.ac.uk, Password: XI5oUUKC. Microscopy data reported in this paper will be

shared by the lead contact upon request. All data reported in this paper will be shared by the lead contact upon request. This paper does not report original code. Any additional information required to reanalyze the data reported in this paper is available from the lead contact upon request.

## *Plasmids*

The vector encoding the lysosomal calcium sensor LAMP2-GCaMP6s (pBoBi-hLAMP2-C-GC6s) was obtained from Addgene (Addgene #154151). The lentiviral packaging vector pΔ-NRF Gag-Pol-Tat-Rev and the pseudotyping vector pMD2.G VSV-G were kindly provided by Prof. Judd Franklin Hultquist of Northwestern University. The lentiviral vector used for lysosomal immunoprecipitation pLJC5-TMEM192-3xHA (Addgene #102930)[61] was kindly provided by Dr. Ali Ghoochani and Prof. Monther Abu-Remaileh of Stanford University. The pCAGGS mitoKeima construct[114] was kindly provided by Dr. Huihui Li and Prof. Ken Nakamura of the Gladstone Institutes. The mouse Lgals3bp-GFP construct was cloned by Gibson Assembly. Mouse Lgals3bp was cloned from Neuro-2a cDNA using Q5 polymerase following the manufacturer's instructions, annealing at 61.2°C with the forward primer caagcttcgaattcagggacATGGCTCTCCTGTGGCTC and the reverse primer cctgtggagccggtggagccCACCATGTCAGTGGAGTTAG. The pEGFP-N3 backbone was subcloned from the LAMP1-mGFP plasmid (Addgene #34831)[115] using the forward primer GGCTCCACCGGCTCCACA and the reverse primer GTCCCTGAATTCGAAGCTTGAGCTC. Gibson Assembly was completed using the NEBuilder HiFi DNA Assembly Master Mix (NEB # E2621L), following the manufacturer's instructions.

## *Neuro-2a Cell Culture*

The murine, male neuroblastoma cell line Neuro-2a was previously modified by introducing transgenic, full-length human apoE3 or apoE4 (herein referred to as apoE3 and apoE4, respectively)[82]. The parental cell line without human apoE expression is referred to as apoE$^{-/-}$, referring to its human apoE genotype. Notably, the murine *Apoe* gene is intact in these cells. Neuro-2a cells were cultured in sterile-filtered minimum essential medium + GlutaMAX (MEM, ThermoFisher #41090-036) supplemented with 10% fetal bovine serum (FBS, ThermoFisher #A31605-02), 1X non-essential amino acids (NEAA, ThermoFisher #11140050), and 1 mM

sodium pyruvate (ThermoFisher, #11360070). Cells were passaged using Accutase (Fisher Scientific, #NC9839010) and used between passages 5-10.

### *Lipofectamine Transfection*

Cells were transfected using Lipofectamine 2000 (ThermoFisher #11668019) following the manufacturer's protocols. Cells were cultured to 70% confluency prior to transfection. For transient transfection, DNA was diluted in OptiMEM to 32 ng/µL and gently mixed. Lipofectamine 2000 was similarly diluted in OptiMEM to 8%, and both mixtures incubated for 5 minutes at room temperature. Following the 5 minutes, DNA-OptiMEM and Lipofectamine-OptiMEM mixtures were combined 1:1, gently mixed, and incubated for 20 minutes at room temperature. The transfection mixture was subsequently added to the cells at a 1:6 mixture-to-media ratio, and the cells transfected overnight. The media was replaced the following day, and the cells were subsequently used for experiments. For siRNA knockdown, we targeted the following genes with the indicated siRNAs (available from ThermoFisher): APOE (AM16708_41598), *App* (s62516), *Lgals3bp* (AM16708_162469), *Mapt* (s70123), *Psen2* (AM16708_68876), scramble control (4390844), and *Tmed5* (AM16703_83238). siRNAs were diluted in OptiMEM to 0.5 µM, and Lipofectamine RNAi Max (ThermoFisher #13778150) diluted in OptiMEM to 5%. siRNA and Lipofectamine mixtures were left for 5 minutes before being combined, and incubated for 20 minutes at room temperature. Following incubation, transfection mixtures were added to the wells at a final concentration of 10% v/v. The cells were first transfected overnight, followed by a complete medium exchange and a second subsequent transfection. The cells were used for experiments after 48 hours knockdown in total.

### *RNA extraction, cDNA synthesis and RT-qPCR*

We used RT-qPCR to quantify the knockdown efficiencies of our siRNAs. Following 48 hours knockdown, RNA was extracted using the RNeasy Kit (Qiagen #74106), following manufacturers' instructions, supplementing RLT buffer with β-mercaptoethanol, homogenizing samples by vortexing and without performing gDNA digestion. cDNA was reverse transcribed using the Superscript IV kit (ThermoFisher #18090010), using 1 µg RNA as template, a 0.5:0.5 mixture of Oligo d(T) and random hexamers for priming. The reaction was performed as follows: 10 minutes hexamer annealing at 23°C, 10 minutes amplification at

55°C, and 10 minutes inactivation at 80°C. Reverse-transcribed cDNA was diluted 1:10 with water. RT-qPCR was run using Power SYBR Green PCR Master Mix (Thermo Fisher #4367659) to detect APOE as previously described,[120] and TaqMan (ThermoFisher #4444963) to detect *App* (Mm01344172_m1), *Hprt* (housekeeping control; Mm01545399_m1), *Lgals3bp* (Mm00478303_m1), *Mapt* (Mm00521988_m1), *Psen2* (Mm00448405_m1), and *Tmed5* (Mm00547008_m1). RT-qPCR reactions were performed on a CFX Opus 96 real-time PCR system (BioRad) with the following cycling parameters: [95°C, 10:00],40x[95°C, 0:15; 60°C, 1:00] for SYBR reactions, [50°C, 2:00; 95°C, 10:00],40x[95°C, 0:15; 60°C, 1:00] for TaqMan reactions. Expression levels were analyzed by the $2^{-\Delta\Delta Ct}$ approach, using *Hprt* as a housekeeping gene and scramble control samples as the treatment control.

## *Immunofluorescence and Confocal Microscopy*

Neuro-2a cells were seeded onto poly-L-lysine-coated (Sigma #P4707) 12 mm glass coverslips for confocal microscopy and cultured as previously described. Cells were washed once with PBS (Corning #21-030-CV) before they were fixed with 4% paraformaldehyde (Sigma #F8775). For lysosomal immunostaining, cells were washed three times with PBS, and simultaneously permeabilized and blocked for 1 hour at room temperature in a saponin-based blocking buffer (BB-S; PBS with 1% BSA, 0.05% Saponin, 50 mM $NH_4Cl$, and 1% $NaN_3$). The cells were stained with mouse anti-HA antibodies (BioLegend #901501) diluted 1:1000, rat anti-mouse Lamp1 antibodies (SantaCruz #sc-19992) diluted 1:100, mouse anti-human LAMP1 antibodies (SantaCruz #sc-20011) diluted 1:800, or rabbit anti-phospho-Tau(S202/T205) (ABclonal #AP0894) diluted 1:1000 in BB-S overnight at 4ºC, washed three times with PBS, and stained with either anti-mouse Alexa488- (ThermoFisher #A11001)-, anti-rabbit Alexa488 (ThermoFisher #A21206)-, anti-mouse Alexa555 (#A31570)-, anti-rabbit Alexa555 (ThermoFisher #A21428)-, or anti-rat fluorescein (Vector #FI-4000)-conjugated secondary antibodies diluted 1:500 in BB-S for 2 hours at room temperature. For iPSC=derived neuron immunostaining, cells were similarly fixed in 4% PFA for 15 minutes, and washed once with PBS. Cere washed once with washing buffer (PBS with 0.1% Tween-20), and blocked with blocking solution (PBS with 10% donkey serum and 0.5% Triton-X) for 1 hour. Cells were stained overnight at 4°C with rabbit anti-GABA (ThermoFisher #PA5-32241) diluted 1:1000 and mouse anti-TuJ (Promega #G712A) diluted 1:1000 in PBS with 1% donkey serum. Cells were washed twice with washing buffer, and

stained with aforementioned secondary antibodies for 1 hour in PBS with 1% donkey serum. Cells were again washed twice with washing buffer. Nuclei were subsequently stained for by incubation with 200 ng/mL Hoechst 33342 (ThermoFisher #H3570) diluted in PBS for 30 minutes at room temperature. The samples were washed three times with PBS and mounted onto Micro Slides (VWR #48311-703) using Cytoseal™ 60 (VWR #8310-4). Images were captured using a confocal laser scanning microscope (Zeiss LSM880) fitted with a Plan-Apochromat 63x/1.4 Oil DIC M27 objective and PMT detector. Nuclei were imaged by excitation at 405 nm and detection between 410-507 nm, with the pinhole set to 1.36 AU. The AlexaFluor488-stained lysosomal tags were imaged by excitation at 488 nm and detection between 493-630 nm, with the pinhole set to 0.43 AU. Pixel scaling was set to 70 nm to capture lysosomal structures.

### *Lysotracker Imaging*

The lysosomal expanse of the Neuro-2a cells was determined using the Lysotracker probe. Neuro-2a cells were seeded into live-cell imaging chambers (ibidi #80806) at a density of $2*10^5$ cells/mL. The media was exchanged for fresh media on day 2 of culture. On day 3, the cells were stained with Lysotracker Red DND-99 (ThermoFisher #L7528) diluted 1:10,000 to label acidic endolysosomes and CellMask™ Deep Red Plasma Membrane Stain (ThermoFisher #C10046) diluted 1:1000 to label the plasma membrane. The cells were loaded for 30 minutes at 37ºC before being chased in culture media not containing staining reagents. The cells were transferred to a confocal laser scanning microscope (Zeiss LSM880) fitted with a Plan-Apochromat 63x/1.4 Oil DIC M27 objective and PMT detector, with its incubation chamber pre-heated to 37ºC and atmosphere filled with 5% $CO_2$. Lysotracker staining was imaged by excitation at 561 nm and detection between 566-639 nm, with the pinhole set to 0.81 AU. CellMask staining was imaged by excitation at 633 nm and detection between 639-759 nm, with the pinhole set to 0.93 AU. Pixel scaling was set to 90 nm to capture lysosomal structures. Image analysis was performed in Fiji. The CellMask channel was used to manually draw regions of interest (ROIs) delimiting individual cells, and the roiManager Measure function used to measure the Lysotracker staining intensity of each cell. The results shown were obtained from three distinct biological and technical replicate experiments.

### *pH Measurements using Oregon Green*

The lysosomal pH was accurately determined using the Oregon Green probe. Neuro-2a cells were seeded into live-cell imaging chambers (ibidi #80806) at a density of $2*10^5$ cells/mL. On day 3, the cells were loaded with 500 µg/mL OregonGreen™ 488; Dextran 70,000 MW (ThermoFisher #D7172) overnight. The following day, the cells were chased in culture medium for 1 hour, before 0.1% DMSO (Sigma #D2650) or 200 nM Bafilomycin A1 (FisherScientific #AAJ61835MCR) was added for another hour. The cells were transferred to a confocal laser scanning microscope (Zeiss LSM880) fitted with a Plan-Apochromat 63x/1.4 Oil DIC M27 objective and PMT detector. pH-insensitive, reference OregonGreen™ 488 staining was imaged by excitation at 458 nm and detection between 495-605 nm. pH-sensitive OregonGreen™ 488 staining was imaged by excitation at 488 nm and detection between 495-605 nm. The pinhole was set to 1.14 AU, and pixel scaling set to 135 nm to capture lysosomal structures. After capturing 7 images of each condition, the lysosomes were pH-clamped using the Intracellular pH Calibration Buffer Kit (ThermoFisher #P35379), with its range expanded to include 10 different pH values ranging from pH 3.60 to pH 7.50, adjusting the buffer pH with HCl. The buffer kit was used following the manufacturer's instructions, adding buffers starting at pH 7.50 and progressively adding more acidic buffers. One calibration image was captured for each pH buffer. Image analysis was performed in Fiji. The CellMask channel was used to manually draw single regions of interest (ROIs) delimiting cells. A mask was generated of endosomes by using the 456 nm reference channel. A minimum filter was first applied followed by a maximum filter (radius=3). The Li AutoThreshold function was used to create a binary mask of lysosomes, followed by a dilation of the cell mask using EDM Binary Operations (iterations=3). The Watershed function was used to divide lysosome clusters, and the mask used to create a region of interest. The region of interest as split into its individual constituents, and the intensity of each individual ROI (endosome) measured from the raw, unprocessed image. The ratio of pH-sensitive to pH-insensitive fluorescence was subsequently calculated for each individual endosome. The same data analysis was performed for the pH-clamped lysosomes, allowing extrapolation from Oregon Green ratios to their respective absolute pH values. The results shown were obtained from three distinct biological and technical replicate experiments.

### *Calcium Imaging using LAMP2-GCaMP6s*

Neuro-2a cells were seeded into live-cell imaging chambers (ibidi #80806) and cells cultured to confluence. Upon reaching confluence, the cells were transiently transfected for 48 hours with the LAMP2-GCaMP6s construct [59] using Lipofectamine 2000 (ThermoFisher #11668019) following the manufacturer's instructions. Following transgene expression, the medium was replaced with $Ca^{2+}$-free standard bath solution (142 mM NaCl, 6 mM KCl, 2 mM $MgCl_2$, 5.5 mM Glucose, 1 mM EGTA, 10 mM HEPES, pH 7.4). Cells were transferred to a Zeiss LSM880 confocal microscope fitted with a Plan-Apochromat 63x/1.4 Oil DIC M27 objective and an Airyscan detector, preequilibrated to 37°C and 5% $CO_2$. Calcium-bound GCaMP6s was imaged by excitation at 488 nm and detection between 415-735 nm. To facilitate high-speed imaging while maintaining resolution of lysosomal structures, pixel scaling was set to 130 nm, the pinhole set to 2.31 AU, and images captured every second for 250 seconds. Cells were treated with 200 µM GPN (Cayman #14634) at 50 seconds, and with 4 µM Ionomycin (Cayman #10004974) at 150 seconds. At least three movies of were captured for each technical replicate. Image analysis was performed in Fiji. A region of interest was generated of transfected cells excluding the nuclei, delimiting the area to be analyzed. The fluorescence intensity of each region of interest (cell) was measured over time using the Fiji MultiMeasure function. The results shown were obtained from three distinct biological and technical replicate experiments.

### *Mitophagy Measurements using mtKeima*

Neuro-2a cells were seeded into live-cell imaging chambers (ibidi #80806) at a density of $2*10^5$ cells/mL, and cells cultured to 70% confluence. Upon reaching 70% confluence, the cells were transfected with the mtKeima construct[114,121] using Lipofectamine 2000 (ThermoFisher #11668019) following the manufacturer's instructions. The cells were transfected overnight, and media changed the next day. Fresh media was added alongside compounds for treatment, including 0.1% DMSO, 10 µM FCCP (Sigma #SML2959), and 200 nM Bafilomycin A1. The cells were incubated for 30 minutes prior to imaging. The cells were transferred to a confocal laser scanning microscope (Zeiss LSM880) fitted with a Plan-Apochromat 63x/1.4 Oil DIC M27 objective and PMT detector, with its incubation chamber pre-heated to 37ºC and atmosphere filled with 5% $CO_2$. Neutral mtKeima was imaged by excitation at 488 nm and detection between 600-708 nm, while simultaneously capturing transmitted light. Acidic mtKeima was imaged by excitation at 514 nm and

detection between 544-680 nm. The pinhole was set to 0.92 AU, and pixel scaling set to 90 nm to capture mitochondrial structures. Five images were captured for each condition. Image analysis was performed in Fiji. A region of interest was generated of transfected cells based on the transmitted light, delimiting the area to be analyzed. A mask was generated of mitochondria by using both mtKeima channels. A minimum filter was first applied followed by a maximum filter (radius=3). The Li AutoThreshold function was used to create a binary mask of lysosomes, followed by a dilation of the cell mask using EDM Binary Operations (iterations=3), watershed, and erosion using EDM Binary Operations (iterations=3). The resulting mask was used to create a region of interest. The region of interest as split into its individual constituents, and the intensity of each individual ROI (mitochondrion) measured from the raw, unprocessed image. The ratio of acidic to neutral mtKeima was calculated for each mitochondrion. The results shown were obtained from three distinct biological and technical replicate experiments.

### *Lentiviral Production*

Lentiviruses were produced as previously described.[113] HEK293T were cultured in DMEM (Corning #10-017-CV) supplemented with 10% fetal bovine serum (FBS, ThermoFisher #A31605-02), 1 mM sodium pyruvate (ThermoFisher, #11360070), and 1X Penicillin-Streptomycin (Corning, #30-002-CI), and used between passages 4-8. On day 1, $6*10^6$ cells were seeded in 50 mL culture medium in 15 cm dishes and allowed to adhere overnight. On day 2, transfection mixtures were prepared by diluting 5 µg lentiviral delivery vector, 3.33 µg Gag-Pol-Tat-Rev packaging construct, and 1.66 µg VSV-G envelope construct in 250 µL serum-free DMEM (Corning #10-017-CV). 30 µL PolyJet In Vitro DNA Transfection Reagent (SignaGen #SL100688) was similarly diluted in 250 µL serum-free DMEM, and incubated at room temperature for 5 minutes. Following the 5 minutes, DNA-DMEM and PolyJet-DMEM mixtures were combined 1:1, gently mixed, and incubated for 25 minutes at room temperature. The transfection mixture was subsequently added dropwise to the cells, plates swirled, and incubated for 72 hours. The supernatant was harvested on day 5. The supernatant was collected, and cellular debris removed by centrifugation at 400g for 5 minutes. The supernatant was subsequently filtered using a 0.45 µm PVDF filter unit, and virions precipitated by adding 8.5% PEG-6000 and 0.3M NaCl followed by 2 hours incubation at 4ºC. Virions were

pelleted by centrifugation at 2700 g for 20 minutes at 4ºC. The supernatant was decanted, virions resuspended in 250 µL PBS, and aliquoted for long-term storage at -80ºC.

### *Lentiviral Transduction*

Neuro-2a cells were transduced by lentiviral spinoculation. Neuro-2a cells were dissociated using Accutase (Fisher Scientific, #NC9839010), and $3*10^4$ cells resuspended in 2 mL media. Polybrene (Millipore #TR-1003-G) was added to the cells to a final concentration of 8 µg/mL alongside 100 µL concentrated lentivirus, and the cells centrifuged at 1000 g for 1 hour at room temperature. The supernatant was aspirated, cells resuspended in 2 mL Neuro-2a media (described in Neuro-2a Cell Culture section) and seeded in a single well of a 6-well tissue culture plate. The cells were cultured for 48 hours post-transduction before selecting for transduced cells using 2 µg/mL Puromycin (ThermoFisher #A1113802) for 3 days. Following antibiotic selection, the polyclonal cells were passaged and expanded once before being frozen for further experiments.

### *Lysosomal Immunoprecipitation*

Lysosomal immunoprecipitation was performed as previously described[61] with minor alterations. Neuro-2a cells with each combination of apoE genotype (apoE$^{-/-}$, apoE3, or apoE4) and lysosomal tag integration (background or LysoIP-tagged) were seeded in duplicate at a density of $1*10^6$ cells/15 cm dish. To distinguish intrinsically lysosomal proteins from lysosomal cargo destined for degradation, two 15 cm dishes of LysoIP-tagged apoE$^{-/-}$, apoE3, and apoE4 Neuro-2a cells were treated with 200 nM Bafilomycin A1 (ThermoFisher #AAJ61835MCR) for 3 hours, preventing lysosomal degradation and enriching for lysosomal cargo. To harvest lysosomes, each sample was individually processed from beginning to lysis. All following steps were performed on ice or at 4ºC ambient temperature, unless otherwise stated. Magnetic anti-HA beads (ThermoFisher #88837) were washed twice with KPBS (136 mM KCl, 10 mM $KH_2PO_4$, pH adjusted to 7.25). Culture media was quickly decanted and rinsed twice with ice-cold KPBS. Cells were collected by scraping and transferred to microfuge tubes. Cells were pelleted by centrifugation (1000g, 2 min), and the supernatant aspirated. The cells were next resuspended in 950 µL KPBS, and 25 µL cell suspension aliquoted into Protein LoBind tubes for whole-cell analysis. The remaining 925 µL cell suspension was homogenized upon passing the entire volume through a 20G needle 10 times, and efficient release of cellular organelles assessed under

a phase contrast microscope. The homogenate was transferred to a new microcentrifuge tube and centrifuged (1000g, 2 min) to pellet the plasma membrane. The supernatant was transferred to a new microcentrifuge tube containing 150 µL magnetic anti-HA beads and mixed once by pipetting. The organelles and beads were rocked at 1200 rpm for 3 minutes and transferred to a magnet for washing. The beads were incubated on the magnet for 25 seconds before the supernatant was aspirated and replaced with fresh KPBS. The beads were rocked at 1200 rpm for 10 seconds and returned to the magnet. These washes were repeated three times, transferring the cells to Protein LoBind tubes for the final wash. Upon aspirating the KPBS following the final wash, 300 µL modified SP3 lysis buffer[122] (50 mM Tris-HCl, 50 mM NaCl, 1% SDS, 1% NP-40, 1% Tween 20, 1% Glycerol, 1% Sodium Deoxycholate, 5 mM EDTA, 5 mM Dithiothreitol, 5 KU Benzonase, 1 Complete protease inhibitor; modified by excluding Triton X-100) was added to the input and bead samples. Upon finishing processing all samples, the samples were lysed by rocking at 65ºC for 30 min at 1200 rpm. LysoIP samples were placed on the magnet for 25 seconds, and the supernatant transferred to fresh Protein LoBind tubes to remove magnetic beads. The samples were alkylated by adding chloracetamide (final concentration 10 mM) and shielded from light for 30 minutes. The alkylated samples were vortexed, solubilized on ice for 20 minutes, and centrifuged at 16000g for 10 minutes. The soluble supernatant was transferred to new tubes, and -20ºC acetone added in four-fold volume to precipitate protein. The samples were briefly vortexed and incubated at -80ºC for 1 hour. Proteins were pelleted by centrifugation (2000 g, 15 min), and the pellet washed twice with -20ºC acetone. The samples were stored at -80ºC until mass spectrometric analysis.

### *Mass Spectrometry*

Dry, digested peptides, were resuspended in 0.1% FA and separated using Thermo EASY-nLC 1200 nano liquid chromatography setup. Separation was performed using a 15 cm long Bruker PepSep column with a 150 µm inner diameter packed with 1.5um Reprosil Saphir C18 particles. Mobile phase A was composed of a 0.1% formic acid solution, while mobile phase B was composed of 0.1% formic acid with 80% acetonitrile. Samples were loaded onto the column at the maximum flow rate possible with an upper pressure limit of 300 bar, with the gradient performed using a stable flow of 600 nl/min. For LysoIP samples, mobile phase began at 2%, before increasing to 30% over 70 mins. Mobile phase B then increased to 35% over 8 minutes before

increasing to 90% B over 2 minutes and finishing with a wash at 90% B for 10 minutes. The gradient required a total time of 90 minutes. For APMS samples, mobile phase began at 4% B before increasing to 35% over 44 minutes. Mobile phase B then increased to 45% over 5 minutes before increasing to 88% B over 1 minute and finishing with a wash at 88% for 10 mins. The gradient for APMS samples required a total time of 60 minutes.

Eluting peptides were ionized using electrospray ionization from a PepSep stainless steel emitter and analyzed using a Thermo Orbitrap Fusion Lumos mass spectrometer. For LysoIP samples acquisition was performed in a data-independent (DIA) manner with a single survey scan from 350-1200 m/z at 120,000 resolution, followed by 40 variable window (**Supplementary Table 1**) MS2 scans at 30,000 resolution with stepped HCD using 32 +/- 5 NCE. Survey scans utilized an AGC target of 4e5 with maximum injection time set to "Auto", while MS2 scan AGC target was set to 5e4 with a maximum injection time of 54 ms. All scans were taken in the Orbitrap. For APMS samples, acquisition was performed in a data-dependent (DDA) manner. Survey scans were taken from 350-1350 m/z at a resolution of 240,000, with a normalized AGC target of 250%, and a maximum injection time 50 ms. Dependent MS2 scans were collected in the ion trap from 200-1200 m/z using the "rapid" scan speed, with a normalized AGC target of 300%, a "dynamic" maximum injection time, and an isolation window of 0.7 m/z. Ions were activated using HCD with 32 NCE. Only ions with charge state 2-5 were selected for fragmentation and ions were excluded with a 10 ppm tolerance for 20 seconds after being isolated for MS2 scans twice. MS system suitability was monitored with QCloud2.[123]

For APMS samples, raw files were searched in MaxQuant using default parameters against a full reviewed mouse proteome including isoforms (downloaded from Uniprot on June 6, 2022) to which human APOE and TMEM192 proteins were added. The evidence.txt output table from that search was then used to generate the three tables necessary for SAINTexpress scoring (baits, preys, and interactions) using the artmsEvidenceToSaintExpress function from the artMS package (release 3.17) in R (version 4.1.1). Two sets of bait, prey, and interaction tables were generated, one using spectral counts and the other using intensity, with GFP samples set as the control group. Interactions were scored using SAINTexpress (version 3.6.3).

Protein interactions were identified as significant if they resulted in a BFDR < 0.05 in either spectral count- or intensity-based SAINT analysis, and the prey protein was observed in all three replicates of that apoE-bait group (e.g., all Lgals3bp-GFP/apoE3, or all Lgals3bp-GFP/apoE4 samples). For these significant interactors we calculated protein fold change and significance when comparing the two alleles (Lgals3bp-GFP/apoE3 vs. Lgals3bp-GFP/apoE4) using the LFQ intensity from the proteinGroups.txt output table from MaxQuant. The identified Lgals3bp interaction partners and their quantification between apoE alleles are provided in **Supplementary Table 3**.

For LysoIP samples, the resulting raw files were searched using directDIA in Spectronaut against a full reviewed mouse proteome including isoforms (downloaded from Uniprot on June 6, 2022) to which human APOE and TMEM192 proteins were added. Default search parameters were used without cross-run normalization or imputation. The resulting MSstats-formatted report was then used to summarize abundance at the protein level using Tukey's median polish after median normalization of peptide features [124]. Proteins were annotated as being lysosomal if they fulfilled one of two conditions: Either they were detected in three tagged replicates but undetected in untagged controls, or they were more than 2-fold enriched in lysosomes over the background, and reaching statistical significance. If proteins were only passing these criteria in Bafilomycin A1-treated samples, they were annotated as being lysosomal cargo. A subset of correlated peptide ions was selected for quantification of TMEM192 protein, to allow for the most accurate normalization of protein abundance to lysosomes. The identified lysosomal proteins, their quantification between alleles and the precursors used for normalization are provided in **Supplementary Table 2**).

Proteins found to be significantly up- or downregulated in apoE4 lysosomes relative to apoE3 or apoE$^{-/-}$ controls were tested for enrichment of Gene Ontology (GO Biological Process, Molecular Function and Cellular Component) terms. The over-representation analysis (ORA) was performed using the enricher function from R package clusterProfiler (version 4.2.2)[125]. The gene ontology terms and annotations were obtained from the R annotation package org.Mm.eg.db (version 3.8.2). Non-redundant GO terms were selected by first constructing a term tree based on distances (1-Jaccard Similarity Coefficients of shared genes in GO database) between the significant terms using the R function hclust. The term tree was then cut at a

specific level (R function cutree, h = 0.99) to identify clusters of redundant gene sets. For results with multiple significant terms belonging to the same cluster, we selected the most significant term (i.e., minimum adjusted p-value).

Principal component analysis and significance testing were performed using base R (svd and t.test functions respectively). Select protein heatmaps were generated using pheatmap package. Lysosomal protein and gene ontology heatmaps were generated using the complexHeatmap package.[126,127] Lysosomal overrepresentation analysis was performed by plotting ratios of ratios. The first ratio is the lysosomal distribution coefficient, calculated as the lysosomal protein abundance relative to the whole-cell protein abundance. Proteins that preferentially localize to lysosomes have a high lysosomal distribution coefficient. Conversely, proteins that prefer cytosolic residency have low lysosomal distribution coefficients. To elucidate whether proteins are overrepresented or underrepresented on apoE4 lysosomes, we divided the lysosomal distribution coefficients of each protein on apoE4 lysosomes by the respective lysosomal distribution coefficient in control cells.

### *Lgals3bp-GFP Affinity Purification*

For each replicate, Neuro-2a cells stably expressing either apoE3 or apoE4 were seeded onto two 15 cm dishes at a density of 400,000 cells, and allowed to grow for 4 days. Each 15 cm dish was transfected with 60 µg DNA using polyJET (SignaGen #SL100688) to deliver expression vectors for GFP or Lgals3bp-GFP, following the manufacturer's instructions. For each vector, three independent biological replicates were prepared. Media was exchanged the following day, and the cells allowed to recover for another three days before harvesting. The subsequent affinity purification was performed as previously described.[28] For each sample, two 15 cm dishes were each rinsed with PBS and scraped in 500 µL NP40 lysis buffer (50 mM Tris-HCl pH 8.0, 150 mM NaCl, 1 mM EDTA pH 8.0, 0.5% Nonidet P40 Substitute, complete protease inhibitor tablet, phosSTOP phosphatase inhibitor tablet) and combined before freezing on dry ice for 20 minutes. Samples were next thawed in a 37°C water bath for lysis until completely thawed, and frozen at -80°C until GFP immunoprecipitation. Frozen samples were again partially thawed at 37°C, and incubated at 4°C on a

tube rotator for 30 minutes. The debris was pelleted by centrifugation (13,000 g, 4°C, 15 minutes) and the supernatant transferred to a 96-well deep well plate and kept on ice until GFP immunoprecipitation.

In addition to lysates, beads and buffers (indicated below) were dispensed into KingFisher 96-well deep-well plates or microplates as appropriate and placed on ice until loaded onto the KingFisher Flex (KFF) Purification System (Thermo Fisher Scientific) for automated processing as follows: GFP-Trap beads (25 µL slurry dispensed in plate 1 only; Cat. #GTMA-10, Chromotek) were equilibrated twice (plates 1,2) with up to 1.0 mL IP Buffer (50 mM Tris–HCl, pH 7.4 at 4 °C, 150 mM NaCl, 1 mM EDTA) supplemented with 0.05% NP40 and incubated with (plate 3) 1.0 mL cell lysate for 2 h. Protein-bound beads were washed three times (plates 4-6) with 1.0 mL IP Buffer supplemented with 0.05% NP40 and then once (plate 7) with 1.0 mL IP buffer before elution. Proteins were eluted from beads (plate 8) in 50 µL 0.05% RapiGest in IP Buffer and combined with residual proteins recovered by rinsing beads (plate 9) in 50 µL IP Buffer for sample processing (below). The KFF is operated in a cold room to maintain a 4°C temperature during immunoprecipitation; however, elution and the final bead rinsing steps were performed using a heat block pre-heated to 23°C. Automated protocol steps were performed using the slow mix speed and the following mix times: 30 seconds for equilibration/wash steps, 2 hours for binding, 35 minutes for elution and 2 minutes for the final bead rinse. Five 30 second bead collection times were used at the end of each step before transferring beads to the next plate.

Proteins from elution and bead rinse steps were combined in a 96-well PCR plate for sample processing as follows: denaturation and reduction at 37°C for 30 m with 2 M urea and 1 mM DTT in 50 mM Tris–HCl pH 8.0, alkylation at room temperature in the dark for 45 m with 3 mM iodoacetamide, and quenching for 10 minutes with 3 mM DTT. Trypsin (0.5 µg/µL; Promega) was added twice (1.0 µL and 0.5 µl) and incubated at 37°C for 4 hours and 2 hours, respectively. Incubations were performed at 37°C in a thermal cycler or at room temperature in a MixMate incubator with shaking at 1,000 rpm. Peptides were acidified with TFA (0.5% final, pH < 2.0) and desalted at room temperature using a BioPureSPE Mini 96-well plate (20 mg PROTO 300 C18; The Nest Group). Briefly, desalting columns were sequentially equilibrated with 0.2 mL 100% methanol; 0.3 mL 80% ACN, 0.1% TFA and 0.3 mL 2% ACN, 0.1% TFA before passing acidified

samples through columns twice and subsequently washed with 2% ACN, 0.1% TFA (0.1 mL and 0.4 mL) and 0.1% FA (0.4 mL, twice). Peptides were eluted twice with 50% ACN, 0.1% FA (60 µL each step) and dried under vacuum centrifugation (CentriVap Concentrator, Labconco). The desalting plate was centrifuged at 2,000 rpm for 2 minutes for initial equilibration steps and 3 minutes for all remaining steps. All buffers were prepared with HPLC or LC-MS grade reagents.

### *Generation of human iPSC-derived neurons*

The human female apoE4 iPSCs and the isogenic apoE3 iPSCs were previously described.[21] Human iPSCs were maintained on Matrigel (Corning #354277) in mTeSR Plus Media (StemCell Technologies #100-0274) and passaged into media supplemented with 10 µM Y-27632 ROCK inhibitor (Tocris #1254) using Accutase (Millipore #scr005). Mixed neurons were generated as reported previously[21], with some modifications. Briefly, iPSCs from 6 100 mm dishes were suspended as single cells in 50 mL KSR medium (80% DMEM #10-566-024, 20% KOSR #10828028, 1X NEAA, 1X GlutaMAX, 0.5X Pen/Strep, 10 µM β-mercaptoethanol) supplemented with 10 µM SB-431542 (Stemgent #04-0010-10), 250 nM LDN-193189 (Stemgent #04-0074), 5 µM IWP2 (Millipore #506072), 100 nM SAG (Millipore #566661), and 10 µM ROCK inhibitors and placed into two T75 flasks to form neurospheres. Neurospheres were fed every second day until day in vitro 7 (DIV7), at which point the KSR small molecule supplements were replaced with 100 ng/mL FGF8 (Peprotech #100-25), 5 µM IWP2, 100 nM SAG, and 250 nM LDN-193189. At DIV14, neuroepithelium was plated down onto two poly-L-lysine (Sigma #4707)/Laminin (ThermoFisher #23017-015)-coated 100 mm cell culture dishes in N2 media (100% DMEM/F12 #11330-032, 0.5X N2 Supplement #17502-048, 1X NEAA, 1X GlutaMAX, 0.5X Pen/Strep) supplemented with 100 ng/mL FGF8 and 100 nM SAG. At DIV21, neuroepithelium was passaged with Accutase, strained through 40 µm filters, counted and centrifuged (200g, 2 min), before they were resuspended in N2/B27 medium (50% DMEM/F12, 50% Neurobasal #21103-049, 0.5X N2 Supplement, 0.5X B27 Supplement (ThermoFisher #17504-044), 1X NEAA, 1X GlutaMAX, 0.5X Pen/Strep) supplemented with 10 ng/mL BDNF (Peprotech #450-02) and 10 ng/mL GDNF (Peprotech #450-10) and seeded at a density of 200,000 cells/mL onto PLL/Laminin-coated glass cover-slips. iPSC-derived neurons were fed twice per week by half feeds, and used at DIV49.

### *Proximity Ligation Assay*

The proximity ligation assay (PLA) was performed following the manufacturer's instructions (Millipore #DUO92101), with minor adaptations to detect lysosomal luminal antigens. Specifically, DIV49 iPSC-derived neurons were washed twice with calcium-containing PBS, fixed with 4% paraformaldehyde for 30 minutes, and washed once with calcium-containing PBS. iPSC-derived neurons were subsequently permeabilized and blocked with BB-S for 1 hour at room temperature. Subsequently, the samples were incubated with the following primary antibodies in BB-S at 4°C overnight: mouse anti-LAMP1 (SantaCruz #sc-20011, diluted 1:800), rabbit anti-LAMP1 (CST #9091S, diluted 1:200), rabbit anti-LGALS3BP (ThermoFisher #10281-1-AP, diluted 1:200), and rabbit anti-TMED5 (ThermoFisher #PA5-141055, diluted 1:500). Coverslips were washed twice in home-made wash buffer A to detect lysosomal antigens (10 mM Tris, 150 mM NaCl, 0.05% Saponin) for 5 minutes, and incubated in a humid chamber with PLA probe solution containing 1X PLUS and MINUS PLA probes against mouse and rabbit primary antibodies for 1 hour at 37°C. Samples were washed twice for 5 minutes with lysosomal wash buffer A, and incubated in 1X ligation solution for 30 minutes in a humid chamber at 37°C. Samples were washed twice for 5 minutes with lysosomal wash buffer A, and incubated in 1X amplification solution for 100 minutes in a humid chamber at 37°C. The samples were finally washed twice for 10 minutes in 1X wash buffer B (200 mM Tris, 100 mM NaCl), once for 1 minute in 0.01X wash buffer B, and mounted in Duolink In Situ Mounting Medium with DAPI on glass slides for confocal microscopy. Images were captured using a confocal laser scanning microscope (Zeiss LSM880) fitted with a Plan-Apochromat 63x/1.4 Oil DIC M27 objective and PMT detector. Nuclei were imaged by excitation at 405 nm and detection between 410-507 nm, with the pinhole set to 1.36 AU. PLA signals were captured using TexasRed excitation/emission settings, with the pinhole set to 1.40 AU. Pixel scaling was set to 70 nm. PLA signals were analyzed in Fiji, drawing region-of-interests around neuronal soma based on PMT and DAPI images, followed by average signal intensity measurements. The experiment was performed in triplicate, using neurons from three different differentiations.

# Supplementary Figures

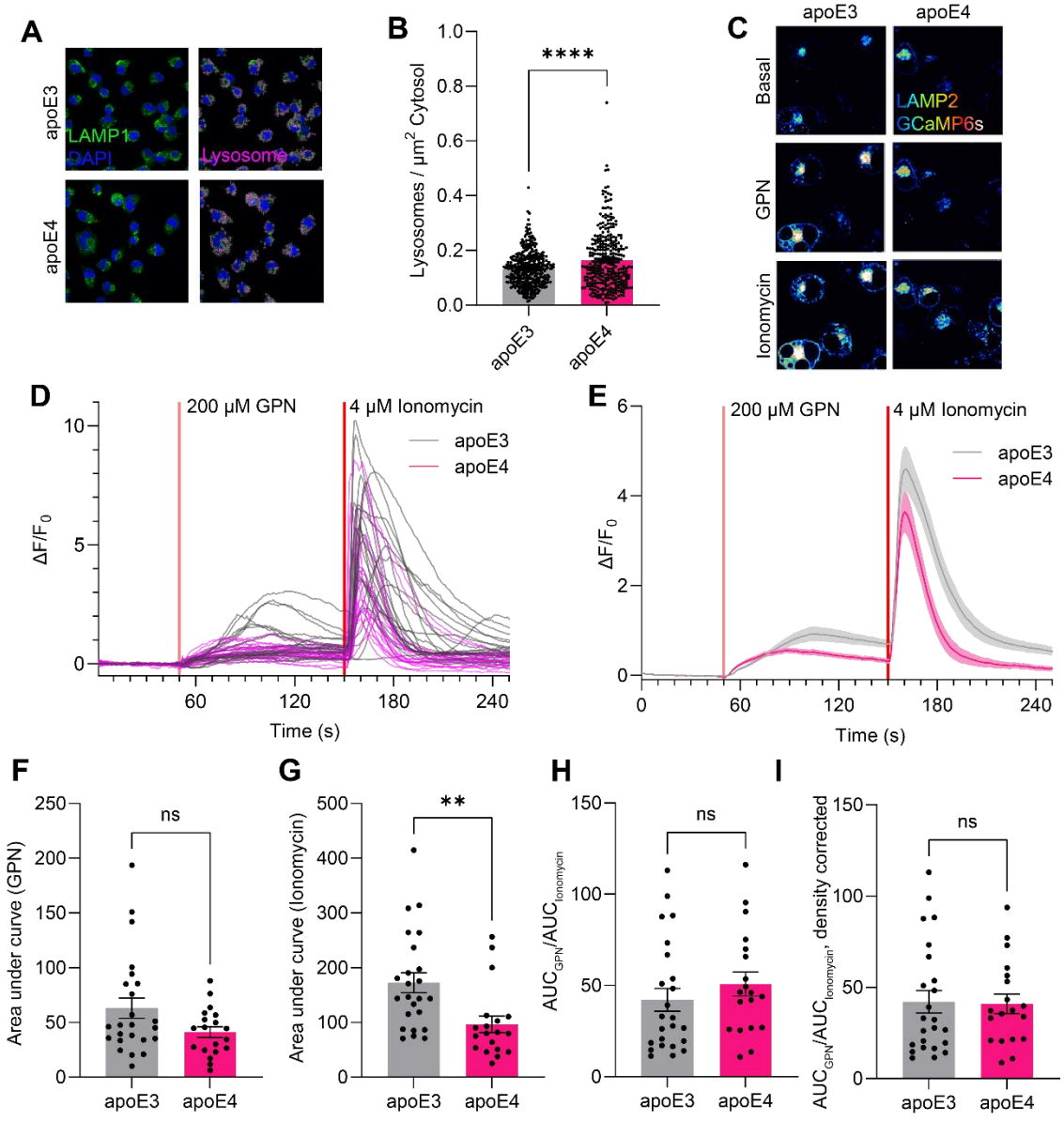


**Figure S1: Lysosomal calcium content.** (**A**) Immunofluorescence of Neuro-2a cells expressing apoE3 or apoE4, stained for the integral lysosomal membrane protein LAMP1. Right panels show puncta identification using Fiji. (**B**) Lysosomal density quantification based on images such as those in panel A. (**C**) LAMP2-GCaMP6s lysosomal calcium measurements in Neuro-2a cells shown at basal states, and upon sequential stimulation using 200 μM GPN to release lysosomal calcium, and 4 μM Ionomycin to release total calcium. (**D**) Single-cell traces for lysosomal calcium release, as shown in panel C. (**E**) Mean

traces of lysosomal calcium release, alongside SEM error bar traces. (**F**) Lysosomal calcium signals, as measured by the area under the curve following GPN and Ionomycin stimulation. (**G**) Total calcium sensitivity of apoE3 and apoE4 cells, as measured by the area under the curve following Ionomycin stimulation. (**H**) Relative lysosomal calcium release, normalized to the calcium sensitivity. (**I**) Relative lysosomal calcium release normalized to the lysosomal density, as calculated in panel B, estimates the lysosomal calcium content of each individual lysosome.

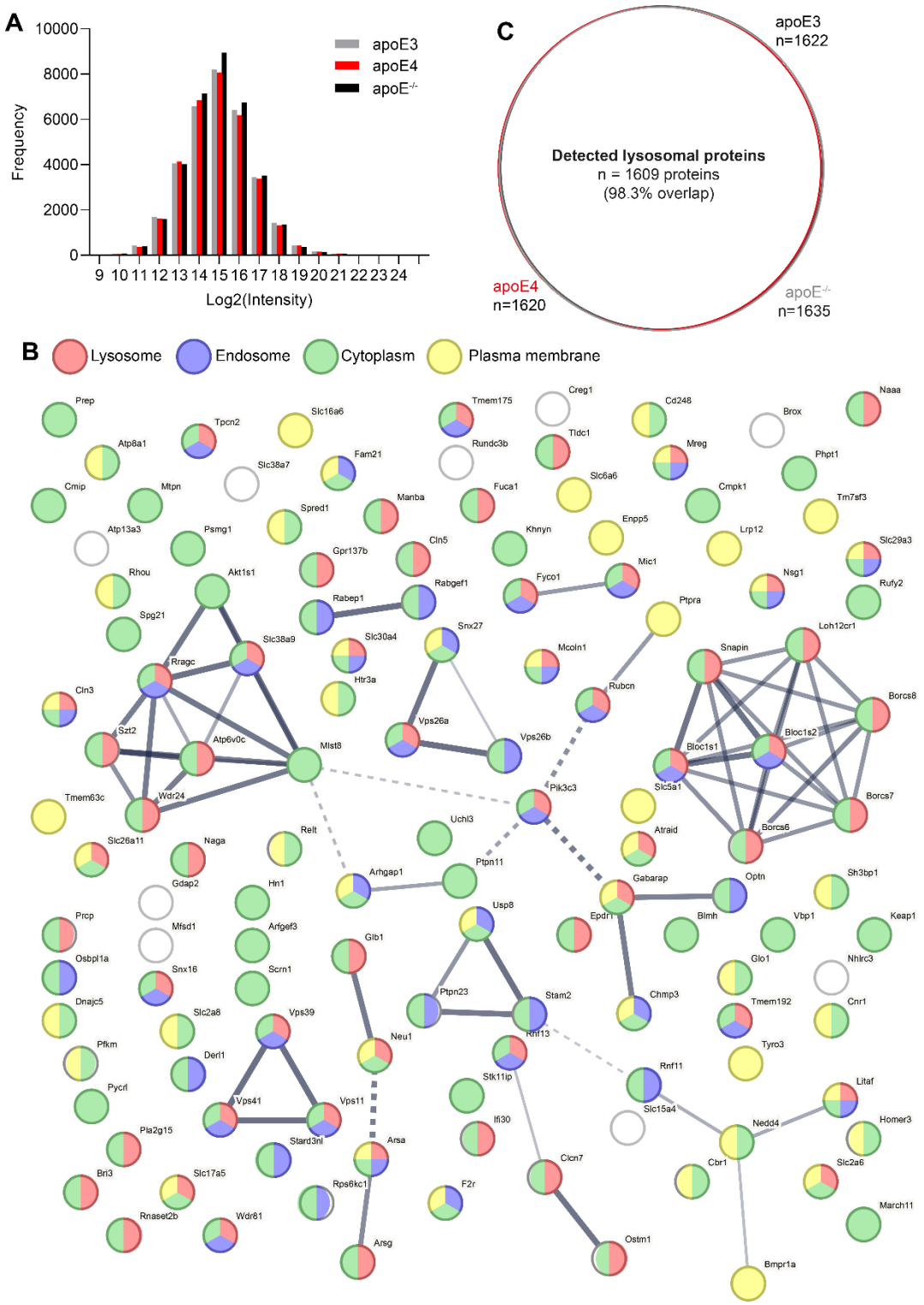


**Figure S2: Lysosomal proteome coverage across apoE genotypes.** (**A**) Histogram of Log2-transformed protein group intensities across all obtained lysosomal proteomes. (**B**) Physical STRING subnetwork of lysosomal proteins either not detected in background samples, present at a two-fold higher intensity in

lysosomal samples across all genotypes, and not annotated with the subcellular localization term "Lysosome" in Uniprot. Nodes are overlaid with associated cellular compartment GO terms. (**C**) Venn diagram of lysosomal proteomes shows high overlap in proteins identified across genotypes.

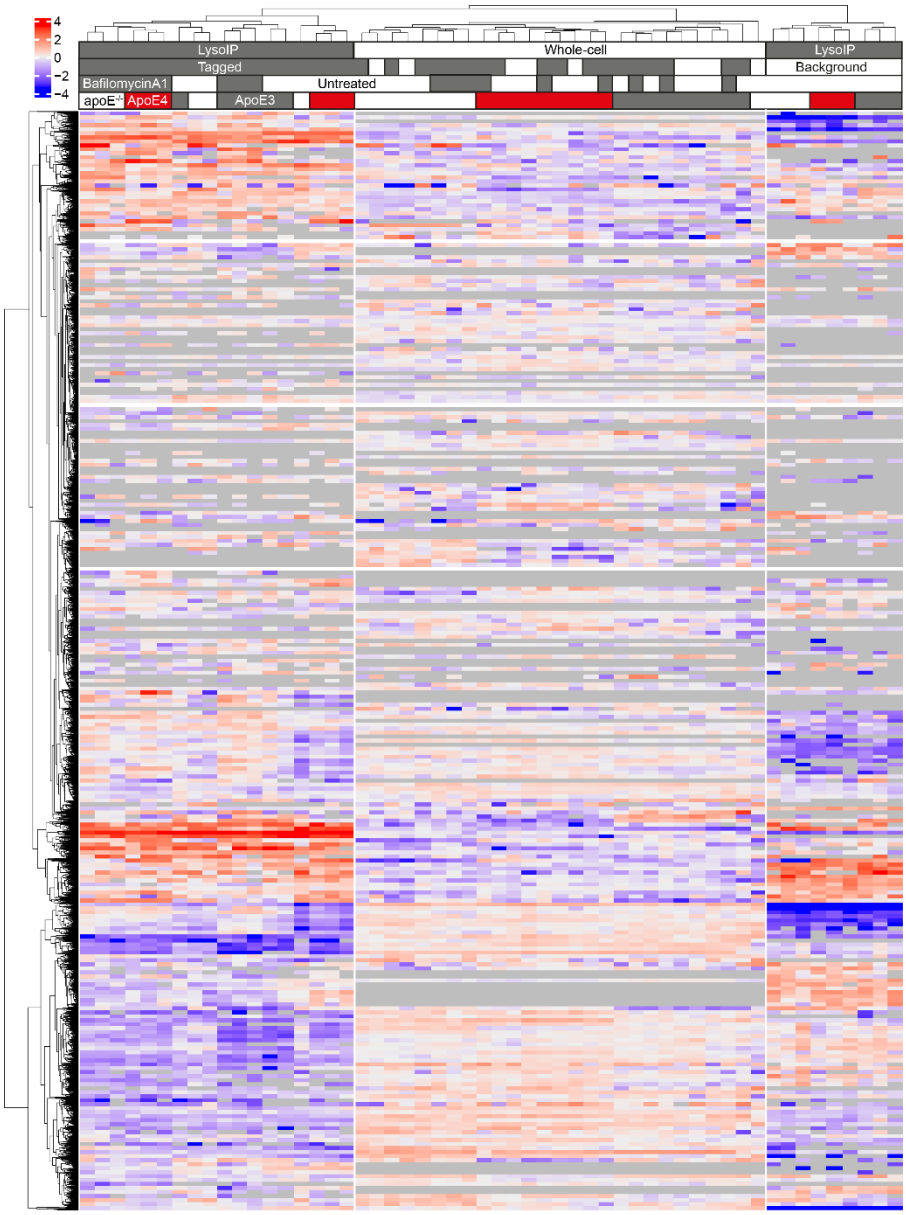


872

**Figure S3: Clustered heat-map of all obtained abundance proteomes.** Heat-map generated from raw intensities of all detected proteins across all samples reveals distinct clustering of LysoIP, whole-cell, and LysoIP background datasets, as well as sub-clustering based on Bafilomycin treatment and apoE genotype.

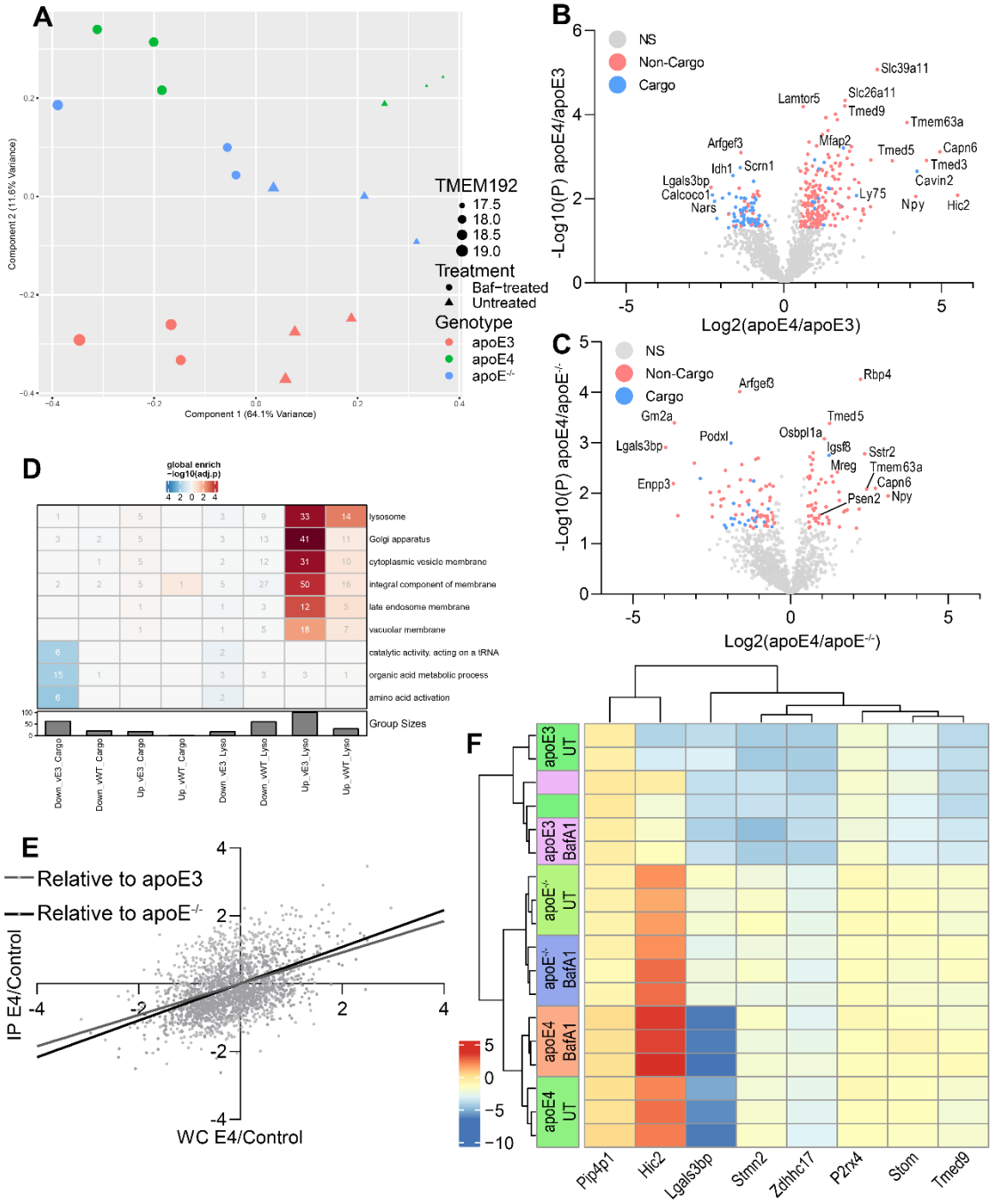

**Figure S4: Proteomic comparisons of apoE lysosomes.** (**A**) Principal component analysis of all lysosomal proteomes separates samples based on Bafilomycin treatment (component 1) and apoE genotype (component 2). (**B**) Volcano plot comparing apoE4 and apoE3 lysosomal proteomes. (**C**) Volcano plot comparing apoE4 and apoE$^{-/-}$ lysosomal proteomes. (**D**) Gene set enrichment analysis of apoE4-associated lysosomal proteome changes of both integral lysosomal proteins and lysosomal cargo. (**E**) Comparison of apoE4-associated changes to whole-cell and lysosomal protein abundances, revealing a high degree of correlation between changed whole-cell protein levels and lysosomal protein levels. Only proteins detected in both sample sets could be plotted. (**F**) Partial least squares-discriminant analysis of lysosomal proteomes reveals proteins separating experimental groups. In particular, apoE4 expression was accompanied by lysosomal Lgals3bp depletion.

875

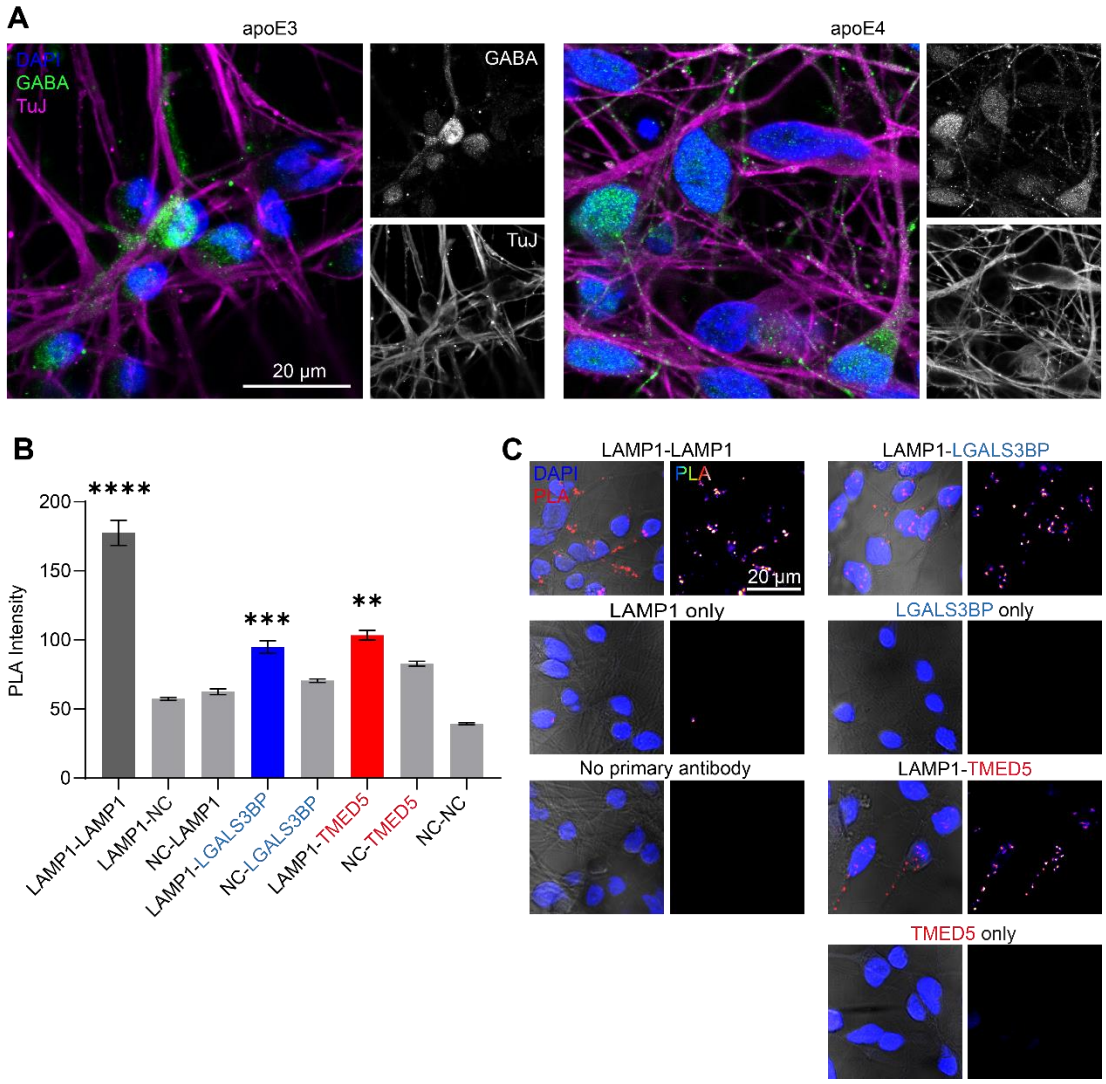


876

**Figure S5: Controls for iPSC-derived neuron proximity ligation assay**. (**A**) Immunofluorescence of neuronal markers following 49 days of differentiation, revealing pure cultures of TuJ$^{+}$ neurons including GABA$^{+}$ interneurons for both genotypes. (**B**) Establishing PLA sensitivities, showing significant signals above negative controls for LAMP1-LAMP1, LAMP1-LGALS3BP, and LAMP1-TMED5 assays. (**C**) Representative images for quantification shown in panel B.

877

878

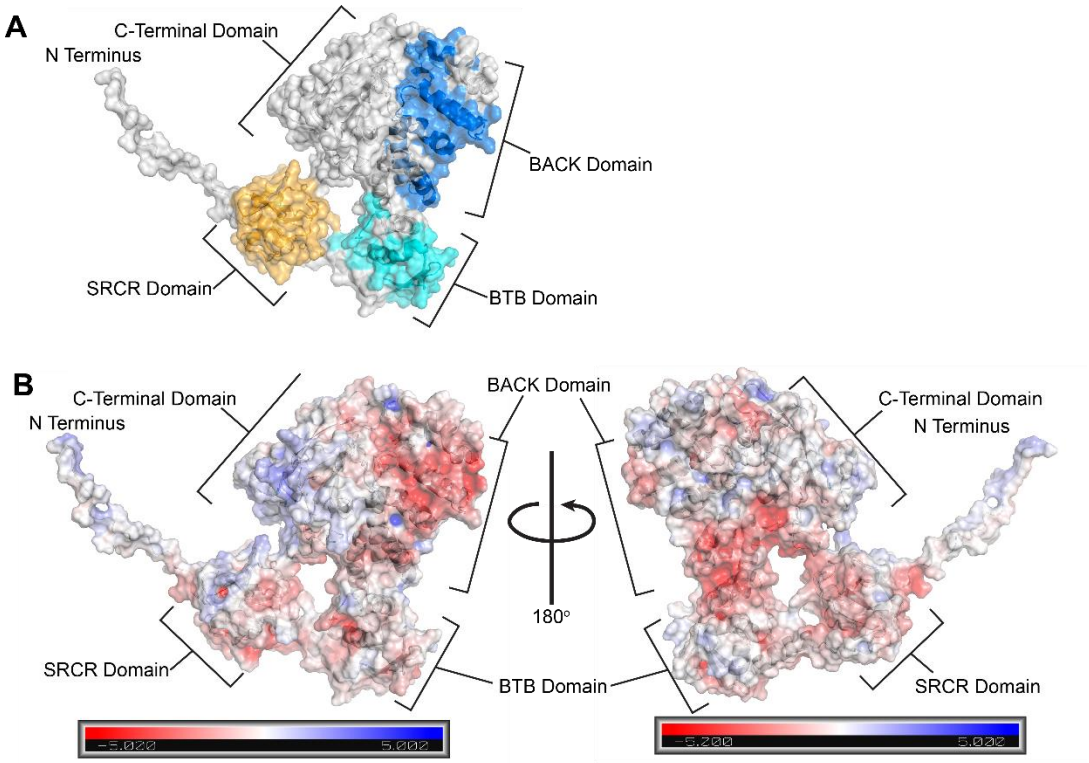


**Figure S6: Structural overview of Lgals3bp**. (**A**) Overall domain architecture of the AutoFold-predicted Lgals3bp structure, highlighting the Lgals3bp domains as specified by Uniprot. (**B**) Electrostatic map of Lgals3bp, as generated using the PyMOL plugin APBS electrostatics [128].

879

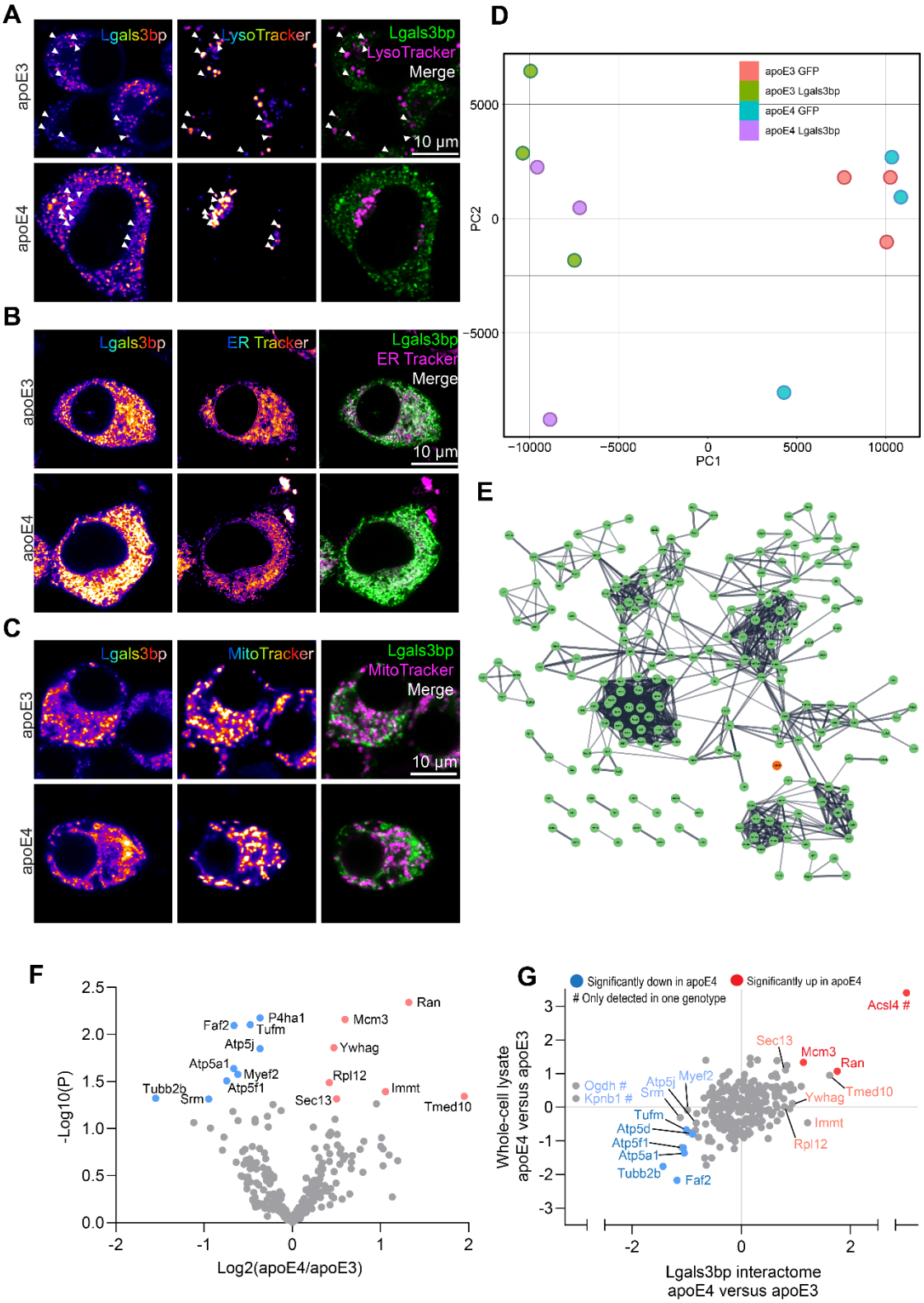
A
apoE3
apoE4
Lgals3bp
LysoTracker
Lgals3bp
LysoTracker
Merge
10 µm
B
Lgals3bp
ER Tracker
Lgals3bp
ER Tracker
Merge
10 µm
C
Lgals3bp
MitoTracker
Lgals3bp
MitoTracker
Merge
10 µm
D
apoE3 GFP
apoE3 Lgals3bp
apoE4 GFP
apoE4 Lgals3bp
PC2
PC1
E
F
-Log10(P)
Log2(apoE4/apoE3)
Ran
Mcm3
P4ha1
Tufm
Faf2
Atp5j
Ywhag
Atp5a1
Myef2
Atp5f1
Rpl12
Tubb2b
Srm
Immt
Sec13
Tmed10
G
Significantly down in apoE4
Significantly up in apoE4
# Only detected in one genotype
Acsl4 #
Sec13
Mcm3
Ran
Ogdh #
Kpnb1 #
Atp5j
Srm
Myef2
Tmed10
Ywhag
Tufm
Immt
Atp5d
Atp5f1
Rpl12
Atp5a1
Tubb2b
Faf2
Whole-cell lysate
apoE4 versus apoE3
Lgals3bp interactome
apoE4 versus apoE3

**Figure S7: The neuronal Lgals3bp interactome.** (**A-C**) The localization of fluorescently tagged Lgals3bp was studied in live Neuro-2a cells stained with either LysoTracker (A), ER Tracker (B), or MitoTracker (C). (**D**) Principal component analysis of affinity-purified proteomes shows clustering of Lgals3bp-GFP-purified samples distinct from GFP background samples (component 1), and slight separation of apoE3 and apoE4 samples (component 2). (**E**) Physical STRING subnetwork of identified Lgals3bp interactors. Lgals3bp is highlighted in red. (**F**) Volcano plot of Lgals3bp interactors changed depending on apoE4 genotype, revealing that most changed interactors are depleted by apoE4 expression. (**G**) Scatter plot showing apoE4-associated changes to whole-cell and Lgals3bp-associated proteins. Each axis shows the geometric mean of the effect size (Log2(apoE4/apoE3) and the statistical significance (-Log10(P)).

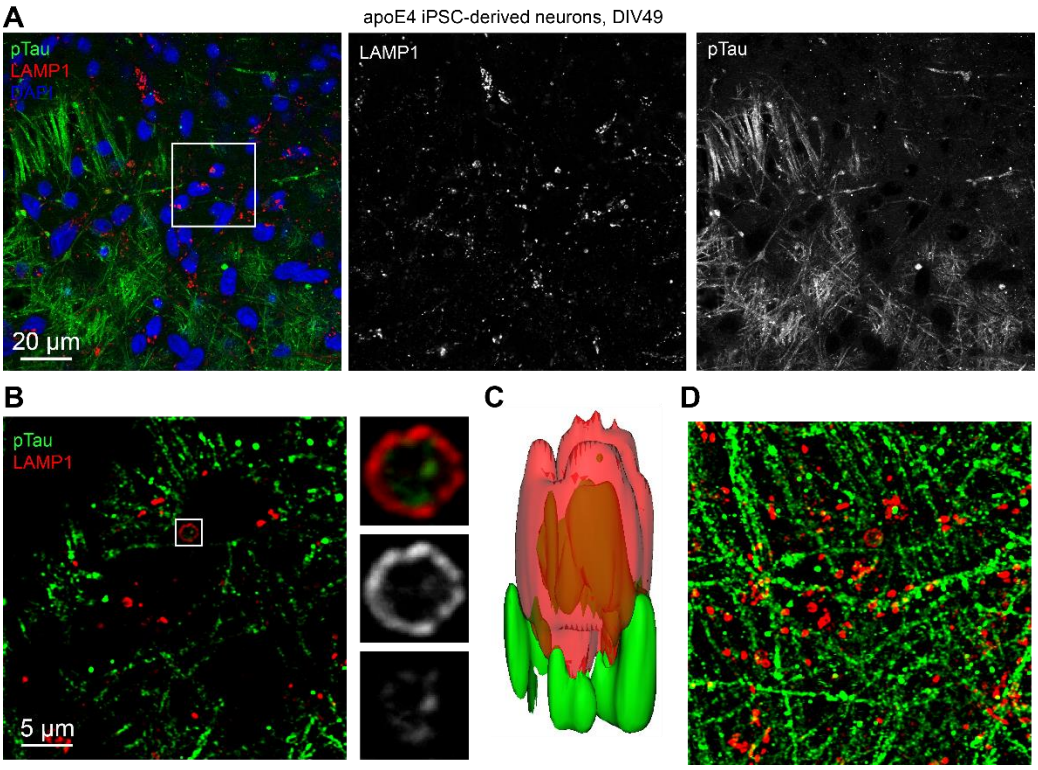


**Figure S8: Hyperphosphorylated tau partially localizes to the lysosomal lumen.** (**A**) Confocal image of human apoE4 iPSC-derived neurons at DIV49, stained for S202/T205 phospho-tau and LAMP1. (**B**) Deconvolved, single-slice zoom-in of the region indicated in panel A, showing two neurons carrying

phospho-Tau-laden lysosomes. The indicated region of a single lysosome carrying pTau is further amplified in the right-hand panels. (**C**) 3D reconstruction of z-stack obtained from the indicated $pTau^+$ lysosome shown in (B), showing complete enclosure of pTau by the lysosomal membrane. A video of the lysosome is shown in supplementary video S1. (**D**) Maximum intensity profile of z-stack shown in (B).

**Video S1: 3D Z-stack of pTau-laden apoE4 lysosome.** Confocal image of human apoE4 iPSC-derived neurons at DIV49 stained for S202/T205 phospho-tau and LAMP1, captured as a z-stack and deconvolved. A snapshot of the video is shown in Figure S8C.

## References


1. The World Health Organization (2021). World failing to address dementia challenge. WHO News. https://www.who.int/news/item/02-09-2021-world-failing-to-address-dementia-challenge.
2. Ballard, C., Gauthier, S., Corbett, A., Brayne, C., Aarsland, D., and Jones, E. (2011). Alzheimer's disease. Lancet *377*, 1019–1031. 10.1016/S0140.
3. Silva, M.V.F., Loures, C.D.M.G., Alves, L.C.V., De Souza, L.C., Borges, K.B.G., and Carvalho, M.D.G. (2019). Alzheimer's disease: Risk factors and potentially protective measures. J Biomed Sci *26*. 10.1186/s12929-019-0524-y.
4. Yamazaki, Y., Painter, M.M., Bu, G., and Kanekiyo, T. (2016). Apolipoprotein E as a Therapeutic Target in Alzheimer's Disease: A Review of Basic Research and Clinical Evidence. CNS Drugs *30*, 773–789. 10.1007/s40263-016-0361-4.
5. Corder, E.H., Saunders, A.M., Gaskell, P.C., Pericak-Vance, M.A., Strittmatter, W.J., Roses, A.D., Haines, J.L., and Pericak-Vance, M.A. (1993). Gene Dose of Apolipoprotein E Type 4 Allele and the Risk of Alzheimer's Disease in Late Onset Families. Science (1979) *261*, 921–923.

6. Michaelson, D.M. (2014). APOE ε4: The most prevalent yet understudied risk factor for Alzheimer's disease. Alzheimer's and Dementia *10*, 861–868. 10.1016/j.jalz.2014.06.015.

7. Langella, S., Barksdale, N.G., Vasquez, D., Aguillon, D., Chen, Y., Su, Y., Acosta-Baena, N., Acosta-Uribe, J., Baena, A.Y., Garcia-Ospina, G., et al. (2023). Effect of apolipoprotein genotype and educational attainment on cognitive function in autosomal dominant Alzheimer's disease. Nat Commun *14*, 5120. 10.1038/s41467-023-40775-z.

8. Levi, O., Jongen-Relo, A.L., Feldon, J., Roses, A.D., and Michaelson, D.M. (2003). ApoE4 impairs hippocampal plasticity isoform-specifically and blocks the environmental stimulation of synaptogenesis and memory. Neurobiol Dis *13*, 273–282. 10.1016/S0969-9961(03)00045-7.

9. Teter, B. (2004). ApoE-Dependent Plasticity in Alzheimer's Disease. J Mol Neurosci *23*, 167–179.

10. Levi, O., Jongen-Relo, A.L., Feldon, J., and Michaelson, D.M. (2005). Brain area- and isoform-specific inhibition of synaptic plasticity by apoE4. J Neurol Sci *229–230*, 241–248. 10.1016/j.jns.2004.11.035.

11. Chen, Y., Durakoglugil, M.S., Xian, X., and Herz, J. (2010). ApoE4 reduces glutamate receptor function and synaptic plasticity by selectively impairing ApoE receptor recycling. Proc Natl Acad Sci U S A *107*, 12011–12016. 10.1073/pnas.0914984107.

12. Koutsodendris, N., Blumenfeld, J., Agrawal, A., Traglia, M., Grone, B., Zilberter, M., Yip, O., Rao, A., Nelson, M.R., Hao, Y., et al. (2023). Neuronal APOE4

removal protects against tau-mediated gliosis, neurodegeneration and myelin deficits. Nat Aging. 10.1038/s43587-023-00368-3.

13. Mishra, S., Blazey, T.M., Holtzman, D.M., Cruchaga, C., Su, Y., Morris, J.C., Benzinger, T.L.S., and Gordon, B.A. (2018). Longitudinal brain imaging in preclinical Alzheimer disease: Impact of APOE ϵ4 genotype. Brain *141*, 1828–1839. 10.1093/brain/awy103.

14. Raber, J., Wong, D., Buttini, M., Orth, M., Bellosta, S., Pitas, R.E., Mahley, R.W., and Mucke, L. (1998). Isoform-specific effects of human apolipoprotein E on brain function revealed in ApoE knockout mice: Increased susceptibility of females. Proc Natl Acad Sci U S A *95*, 10914–10919. 10.1073/pnas.95.18.10914.

15. Hartman, R.E., Wozniak, D.F., Nardi, A., Olney, J.W., Sartorius, L., and Holtzman, D.M. (2001). Behavioral phenotyping of GFAP-ApoE3 and -ApoE4 transgenic mice: ApoE4 mice show profound working memory impairments in the absence of Alzheimer's-like neuropathology. Exp Neurol *170*, 326–344. 10.1006/exnr.2001.7715.

16. Grootendorst, J., Bour, A., Vogel, E., Kelche, C., Sullivan, P.M., Dodart, J.C., Bales, K., and Mathis, C. (2005). Human apoE targeted replacement mouse lines: h-apoE4 and h-apoE3 mice differ on spatial memory performance and avoidance behavior. Behavioural Brain Research *159*, 1–14. 10.1016/j.bbr.2004.09.019.

17. Tong, L.M., Djukic, B., Arnold, C., Gillespie, A.K., Yoon, S.Y., Wang, M.M., Zhang, O., Knoferle, J., Rubenstein, J.L.R., Alvarez-Buylla, A., et al. (2014). Inhibitory interneuron progenitor transplantation restores normal learning and

memory in ApoE4 knock-in mice without or with Aβ accumulation. Journal of Neuroscience *34*, 9506–9515. 10.1523/JNEUROSCI.0693-14.2014.

18. Yamazaki, Y., Liu, C.C., Yamazaki, A., Shue, F., Martens, Y.A., Chen, Y., Qiao, W., Kurti, A., Oue, H., Ren, Y., et al. (2021). Vascular ApoE4 Impairs Behavior by Modulating Gliovascular Function. Neuron *109*, 438-447.e6. 10.1016/j.neuron.2020.11.019.

19. Najm, R., Zalocusky, K.A., Zilberter, M., Yoon, S.Y., Hao, Y., Koutsodendris, N., Nelson, M., Rao, A., Taubes, A., Jones, E.A., et al. (2020). In Vivo Chimeric Alzheimer's Disease Modeling of Apolipoprotein E4 Toxicity in Human Neurons. Cell Rep *32*, 107962. 10.1016/j.celrep.2020.107962.

20. Lin, Y.T., Seo, J., Gao, F., Feldman, H.M., Wen, H.L., Penney, J., Cam, H.P., Gjoneska, E., Raja, W.K., Cheng, J., et al. (2018). APOE4 Causes Widespread Molecular and Cellular Alterations Associated with Alzheimer's Disease Phenotypes in Human iPSC-Derived Brain Cell Types. Neuron *98*, 1141-1154.e7. 10.1016/j.neuron.2018.05.008.

21. Wang, C., Najm, R., Xu, Q., Jeong, D.E., Walker, D., Balestra, M.E., Yoon, S.Y., Yuan, H., Li, G., Miller, Z.A., et al. (2018). Gain of toxic apolipoprotein E4 effects in human iPSC-derived neurons is ameliorated by a small-molecule structure corrector. Nat Med *24*, 647–657. 10.1038/s41591-018-0004-z.

22. Zalocusky, K.A., Najm, R., Taubes, A.L., Hao, Y., Yoon, S.Y., Koutsodendris, N., Nelson, M.R., Rao, A., Bennett, D.A., Bant, J., et al. (2021). Neuronal ApoE upregulates MHC-I expression to drive selective neurodegeneration in Alzheimer's disease. Nat Neurosci *24*, 786–798. 10.1038/s41593-021-00851-3.

23. Prasad, H., and Rao, R. (2018). Amyloid clearance defect in ApoE4 astrocytes is reversed by epigenetic correction of endosomal pH. Proc Natl Acad Sci U S A *115*, E6640–E6649. 10.1073/pnas.1801612115.

24. Blanchard, J.W., Akay, L.A., Davila-Velderrain, J., von Maydell, D., Mathys, H., Davidson, S.M., Effenberger, A., Chen, C.Y., Maner-Smith, K., Hajjar, I., et al. (2022). APOE4 impairs myelination via cholesterol dysregulation in oligodendrocytes. Nature *611*, 769–779. 10.1038/s41586-022-05439-w.

25. Nathan, B.P., Chang, K.C., Bellosta, S., Brisch, E., Ge, N., Mahley, R.W., and Pitas, R.E. (1995). The inhibitory effect of apolipoprotein E4 on neurite outgrowth is associated with microtubule depolymerization. Journal of Biological Chemistry *270*, 19791–19799. 10.1074/jbc.270.34.19791.

26. Muth, C., Hartmann, A., Sepulveda-Falla, D., Glatzel, M., and Krasemann, S. (2019). Phagocytosis of apoptotic cells is specifically upregulated in apoe4 expressing microglia in vitro. Front Cell Neurosci *13*. 10.3389/fncel.2019.00181.

27. Mahley, R.W., and Huang, Y. (2006). Apolipoprotein (apo) E4 and Alzheimer's disease: Unique conformational and biophysical properties of apoE4 can modulate neuropathology. Acta Neurol Scand *114*, 8–14. 10.1111/j.1600-0404.2006.00679.x.

28. Cakir, Z., Lord, S.J., Zhou, Y., Jang, G.M., Polacco, B.J., Eckhardt, M., Jimenez-Morales, D., Newton, B.W., Orr, A.L., Johnson, J.R., et al. (2023). Quantitative Proteomic Analysis Reveals apoE4-Dependent Phosphorylation of the Actin-Regulating Protein VASP. Mol Cell Proteomics *22*, 100541. 10.1016/j.mcpro.2023.100541.

29. Castellano, J.M., Kim, J., Stewart, F.R., Jiang, H., Demattos, R.B., Patterson, B.W., Fagan, A.M., Morris, J.C., Mawuenyega, K.G., Cruchaga, C., et al. (2011). Human apoE Isoforms Differentially Regulate Brain Amyloid-b Peptide Clearance.

30. Deane, R., Sagare, A., Hamm, K., Parisi, M., Lane, S., Finn, M.B., Holtzman, D.M., and Zlokovic, B. V. (2008). apoE isoform-specific disruption of amyloid β peptide clearance from mouse brain. Journal of Clinical Investigation *118*, 4002–4013. 10.1172/JCI36663.

31. Tzioras, M., Davies, C., Newman, A., Jackson, R., and Spires-Jones, T. (2019). APOE at the interface of inflammation, neurodegeneration and pathological protein spread in Alzheimer's disease. Neuropathol Appl Neurobiol *45*, 327–346. 10.1111/nan.12529.

32. Schmukler, E., Solomon, S., Simonovitch, S., Goldshmit, Y., Wolfson, E., Michaelson, D.M., and Pinkas-Kramarski, R. (2020). Altered mitochondrial dynamics and function in APOE4-expressing astrocytes. Cell Death Dis *11*. 10.1038/s41419-020-02776-4.

33. Simonovitch, S., Schmukler, E., Masliah, E., Pinkas-Kramarski, R., and Michaelson, D.M. (2019). The Effects of APOE4 on Mitochondrial Dynamics and Proteins in vivo. Journal of Alzheimer's Disease *70*, 861–875. 10.3233/JAD-190074.

34. Orr, A.L., Kim, C., Jimenez-Morales, D., Newton, B.W., Johnson, J.R., Krogan, N.J., Swaney, D.L., and Mahley, R.W. (2019). Neuronal Apolipoprotein E4 Expression Results in Proteome-Wide Alterations and Compromises Bioenergetic

Capacity by Disrupting Mitochondrial Function. Journal of Alzheimer's Disease *68*, 991–1011. 10.3233/JAD-181184.

35. Xian, X., Pohlkamp, T., Durakoglugil, M.S., Wong, C.H., Rgen, J., Beck, K., Lane-Donovan, C., Plattner, F., and Herz, J. (2018). Reversal of ApoE4-induced recycling block as a novel prevention approach for Alzheimer's disease. 10.7554/eLife.40048.001.

36. Rawat, V., Wang, S., Sima, J., Bar, R., Liraz, O., Gundimeda, U., Parekh, T., Chan, J., Johansson, J.O., Tang, C., et al. (2019). ApoE4 Alters ABCA1 membrane trafficking in astrocytes. Journal of Neuroscience *39*, 9611–9622. 10.1523/JNEUROSCI.1400-19.2019.

37. Narayan, P., Sienski, G., Bonner, J.M., Lin, Y.T., Seo, J., Baru, V., Haque, A., Milo, B., Akay, L.A., Graziosi, A., et al. (2020). PICALM Rescues Endocytic Defects Caused by the Alzheimer's Disease Risk Factor APOE4. Cell Rep *33*. 10.1016/j.celrep.2020.108224.

38. Nuriel, T., Peng, K.Y., Ashok, A., Dillman, A.A., Figueroa, H.Y., Apuzzo, J., Ambat, J., Levy, E., Cookson, M.R., Mathews, P.M., et al. (2017). The endosomal-lysosomal pathway is dysregulated by APOE4 expression in vivo. Front Neurosci *11*, 1–12. 10.3389/fnins.2017.00702.

39. Nakamura, T., Watanabe, A., Fujino, T., Hosono, T., and Michikawa, M. (2009). Apolipoprotein E4 (1-272) fragment is associated with mitochondrial proteins and affects mitochondrial function in neuronal cells. Mol Neurodegener *4*, 1–11. 10.1186/1750-1326-4-35.

40. Chen, H.K., Ji, Z.S., Dodson, S.E., Miranda, R.D., Rosenblum, C.I., Reynolds, I.J., Freedman, S.B., Weisgraber, K.H., Huang, Y., and Mahley, R.W. (2011). Apolipoprotein E4 domain interaction mediates detrimental effects on mitochondria and is a potential therapeutic target for alzheimer disease. Journal of Biological Chemistry *286*, 5215–5221. 10.1074/jbc.M110.151084.

41. Basit, F., van Oppen, L.M.P.E., Schöckel, L., Bossenbroek, H.M., van Emst-De Vries, S.E., Hermeling, J.C.W., Grefte, S., Kopitz, C., Heroult, M., Willems, P.H.G.M., et al. (2017). Mitochondrial complex i inhibition triggers a mitophagy-dependent ROS increase leading to necroptosis and ferroptosis in melanoma cells. Cell Death Dis *8*. 10.1038/cddis.2017.133.

42. Palikaras, K., Princz, A., and Tavernarakis, N. (2019). Mitophagy modulators. In Encyclopedia of Biomedical Gerontology (Elsevier Inc.), pp. 433–446. 10.1016/B978-0-12-801238-3.62137-2.

43. Karch, C.M., and Goate, A.M. (2015). Alzheimer's Disease Risk Genes and Mechanisms of Disease Pathogenesis. Biol Psychiatry *77*, 43–51. 10.1016/j.biopsych.2014.05.006.

44. Hung, C.O.Y., and Livesey, F.J. (2018). Altered gamma-Secretase Processing of APP Disrupts Lysosome and Autophagosome Function in Monogenic Alzheimer's Disease. Cell Rep *25*, 3647–3660. 10.1016/j.celrep.2018.11.095.

45. Gao, S., Casey, A.E., Sargeant, T.J., and Mäkinen, V.P. (2018). Genetic variation within endolysosomal system is associated with late-onset Alzheimer's disease. Brain *141*, 2711–2720. 10.1093/brain/awy197.

46. Zhang, L., Sheng, R., and Qin, Z. (2009). The lysosome and neurodegenerative diseases. Acta Biochim Biophys Sin *41*, 437–445. 10.1093/abbs/gmp031.Review.

47. Leeman, D.S., Hebestreit, K., Ruetz, T., Webb, A.E., McKay, A., Pollina, E.A., Dulken, B.W., Zhao, X., Yeo, R.W., Ho, T.T., et al. (2018). Lysosome activation clears aggregates and enhances quiescent neural stem cell activation during aging. Science (1979) *359*, 1277–1283. 10.1126/science.aag3048.

48. Platt, F.M., D'Azzo, A., Davidson, B.L., Neufeld, E.F., and Tifft, C.J. (2018). Lysosomal storage diseases. Nat Rev Dis Primers *4*, 27. 10.1038/s41572-018-0025-4.

49. Krogsaeter, E., Scotto, A., and Grimm, C. (2022). TRPMLs and TPCs: Targets for lysosomal storage and neurodegenerative disease therapy? Cell Calcium *103*, 102553. 10.1016/j.ceca.2022.102553.

50. Bahr, B.A., and Bendiske, J. (2002). The neuropathogenic contributions of lysosomal dysfunction. J Neurochem *83*, 481–489.

51. Keilani, S., Lun, Y., Stevens, A.C., Williams, H.N., Sjoberg, E.R., Khanna, R., Valenzano, K.J., Checler, F., Buxbaum, J.D., Yanagisawa, K., et al. (2012). Lysosomal dysfunction in a mouse model of sandhoff disease leads to accumulation of ganglioside-bound amyloid-β peptide. Journal of Neuroscience *32*, 5223–5236. 10.1523/JNEUROSCI.4860-11.2012.

52. Guan, J., Mishra, S., Qiu, Y., Shi, J., Trudeau, K., Las, G., Liesa, M., Shirihai, O.S., Connors, L.H., Seldin, D.C., et al. (2014). Lysosomal dysfunction and impaired autophagy underlie the pathogenesis of amyloidogenic light chain-

mediated cardiotoxicity. EMBO Mol Med *6*, 1493–1507. 10.15252/emmm.201404190.

53. Laili, I.N., Nasir, M.H.M., Jufri, N.F., Ibrahim, F.W., and Hamid, A. (2023). Lysosomal dysfunction induced cytosolic vacuolation and increased intracellular amyloid-beta 42 (Aβ42) in human brain endothelial cells (HBEC-5i). Biomedicine and Pharmacotherapy *161*. 10.1016/j.biopha.2023.114501.

54. Li, J., Kanekiyo, T., Shinohara, M., Zhang, Y., LaDu, M.J., Xu, H., and Bu, G. (2012). Differential regulation of amyloid-β endocytic trafficking and lysosomal degradation by apolipoprotein E isoforms. Journal of Biological Chemistry *287*, 44593–44601. 10.1074/jbc.M112.420224.

55. Sannerud, R., Esselens, C., Ejsmont, P., Mattera, R., Rochin, L., Tharkeshwar, A.K., De Baets, G., De wever, V., Habets, R., Baert, V., et al. (2016). Restricted Location of PSEN2/gamma-Secretase Determines Substrate Specificity and Generates an Intracellular Abeta Pool. Cell *166*, 193–208. 10.1016/j.cell.2016.05.020.

56. Lee, J.-H., Yu, W.H., Kumar, A., Lee, S., Mohan, P.S., Peterhoff, C.M., Wolfe, D.M., Martinez-vicente, M., Massey, A.C., Sovak, G., et al. (2010). Lysosomal Proteolysis and Autophagy Require Presenilin 1 and Are Disrupted by Alzheimer-Related PS1 Mutations. Cell *141*, 1146–1158. 10.1016/j.cell.2010.05.008.

57. Fote, G.M., Geller, N.R., Efstathiou, N.E., Hendricks, N., Vavvas, D.G., Reidling, J.C., Thompson, L.M., and Steffan, J.S. (2022). Isoform-dependent lysosomal degradation and internalization of apolipoprotein E requires autophagy proteins. J Cell Sci *135*. 10.1242/jcs.258687.

58. Morgan, A.J., Platt, F.M., Lloyd-Evans, E., and Galione, A. (2011). Molecular mechanisms of endolysosomal Ca 2+ signalling in health and disease. Biochemical Journal *439*, 349–374. 10.1042/BJ20110949.

59. Li, M., Zhang, C.S., Zong, Y., Feng, J.W., Ma, T., Hu, M., Lin, Z., Li, X., Xie, C., Wu, Y., et al. (2019). Transient Receptor Potential V Channels Are Essential for Glucose Sensing by Aldolase and AMPK. Cell Metab *30*, 508-524.e12. 10.1016/j.cmet.2019.05.018.

60. Yuan, Y., Kilpatrick, B.S., Gerndt, S., Bracher, F., Grimm, C., Schapira, A.H., and Patel, S. (2021). The lysosomotrope GPN mobilises Ca2+ from acidic organelles. J Cell Sci *134*. 10.1242/jcs.256578.

61. Abu-Remaileh, M., Wyant, G.A., Kim, C., Laqtom, N.N., Abbasi, M., Chan, S.H., Freinkman, E., and Sabatina, D.M. (2017). Lysosomal metabolomics reveals V-ATPase- and mTOR-dependent mechanisms for the efflux of amino acids from lysosomes. Science (1979) *358*, 4.

62. Zavodszky, E., and Hegde, R.S. (2019). Misfolded GPI-anchored proteins are escorted through the secretory pathway by ER-derived factors. Elife *8*, e46740.

63. Xu, J., Barone, S., Li, H., Holiday, S., Zahedi, K., and Soleimani, M. (2011). Slc26a11, a chloride transporter, localizes with the vacuolar H+-ATPase of A-intercalated cells of the kidney. Kidney Int *80*, 926–937. 10.1038/ki.2011.196.

64. Pires, G., McElligott, S., Drusinsky, S., Halliday, G., Potier, M., Wisniewski, T., and Drummond, E. (2019). Secernin-1 is a novel phosphorylated tau binding protein that accumulates in Alzheimer's disease and not in other tauopathies. Acta Neuropathol Commun *7*, 1–17.

65. Singh, M.K., Richter, S., Beckmann, H., Kientz, M., Nielsen, M., Kno, C., Stierhof, D., Anders, N., Fa, F., Thomann, A., et al. (2018). A single class of ARF GTPase acativated by several pathway-specific ARF-GEFs regulates essential membrane traffic in Arabidopsis. PLoS Genet *14*, 1–36. 10.1371/journal.pgen.1007795.

66. Knoferle, J., Yoon, S.Y., Walker, D., Leung, L., Gillespie, A.K., Tong, L.M., Bien-Ly, N., and Huang, Y. (2014). Apolipoprotein E4 produced in GABAergic interneurons causes learning and memory deficits in mice. Journal of Neuroscience *34*, 14069–14078. 10.1523/JNEUROSCI.2281-14.2014.

67. Koutsodendris, N., Nelson, M.R., Rao, A., and Huang, Y. (2021). Apolipoprotein E and Alzheimer's Disease: Findings, Hypotheses, and Potential Mechanisms. Annu Rev Pathol, 73–99. 10.1146/annurev-pathmechdis-030421-112756.

68. Alam, M.S. (2018). Proximity Ligation Assay (PLA). Curr Protoc Immunol *123*. 10.1002/cpim.58.

69. Barral, D.C., Staiano, L., Guimas Almeida, C., Cutler, D.F., Eden, E.R., Futter, C.E., Galione, A., Marques, A.R.A., Medina, D.L., Napolitano, G., et al. (2022). Current methods to analyze lysosome morphology, positioning, motility and function. Traffic *23*, 238–269. 10.1111/tra.12839.

70. de Araujo, M.E.G., Liebscher, G., Hess, M.W., and Huber, L.A. (2020). Lysosomal size matters. Traffic *21*, 60–75. 10.1111/tra.12714.

71. Fogeron, M.L., Müller, H., Schade, S., Dreher, F., Lehmann, V., Kühnel, A., Scholz, A.K., Kashofer, K., Zerck, A., Fauler, B., et al. (2013). LGALS3BP

regulates centriole biogenesis and centrosome hypertrophy in cancer cells. Nat Commun *4*. 10.1038/ncomms2517.

72. Costa, J., Pronto-Laborinho, A., Pinto, S., Gromicho, M., Bonucci, S., Tranfield, E., Correia, C., Alexandre, B.M., and de Carvalho, M. (2020). Investigating LGALS3BP/90 K glycoprotein in the cerebrospinal fluid of patients with neurological diseases. Sci Rep *10*, 1–9. 10.1038/s41598-020-62592-w.

73. Kyrousi, C., O'Neill, A.C., Brazovskaja, A., He, Z., Kielkowski, P., Coquand, L., Di Giaimo, R., D' Andrea, P., Belka, A., Forero Echeverry, A., et al. (2021). Extracellular LGALS3BP regulates neural progenitor position and relates to human cortical complexity. Nat Commun *12*. 10.1038/s41467-021-26447-w.

74. Song, Y., Wang, M., Tong, H., Tan, Y., Hu, X., Wang, K., and Wan, X. (2021). Plasma exosomes from endometrial cancer patients contain LGALS3BP to promote endometrial cancer progression. Oncogene *40*, 633–646. 10.1038/s41388-020-01555-x.

75. Yap, N.V.L., Whelan, F.J., Bowdish, D.M.E., and Golding, G.B. (2015). The evolution of the scavenger receptor cysteine-rich domain of the class A scavenger receptors. Front Immunol *6*. 10.3389/fimmu.2015.00342.

76. Stogios, P.J., and Privé, G.G. (2004). The BACK domain in BTB-kelch proteins. Trends Biochem Sci *29*, 634–637.

77. Akter, F., Bonini, S., Ponnaiyan, S., Kögler-Mohrbacher, B., Bleibaum, F., Damme, M., Renard, B.Y., and Winter, D. (2023). Multi–Cell Line Analysis of Lysosomal Proteomes Reveals Unique Features and Novel Lysosomal Proteins. Molecular & Cellular Proteomics *22*, 100509. 10.1016/j.mcpro.2023.100509.

78. Martinez-Val, A., Bekker-Jensen, D.B., Steigerwald, S., Koenig, C., Østergaard, O., Mehta, A., Tran, T., Sikorski, K., Torres-Vega, E., Kwasniewicz, E., et al. (2021). Spatial-proteomics reveals phospho-signaling dynamics at subcellular resolution. Nat Commun *12*. 10.1038/s41467-021-27398-y.

79. Szklarczyk, D., Kirsch, R., Koutrouli, M., Nastou, K., Mehryary, F., Hachilif, R., Gable, A.L., Fang, T., Doncheva, N.T., Pyysalo, S., et al. (2023). The STRING database in 2023: protein–protein association networks and functional enrichment analyses for any sequenced genome of interest. Nucleic Acids Res *51*, D638–D646. 10.1093/nar/gkac1000.

80. Oughtred, R., Rust, J., Chang, C., Breitkreutz, B.J., Stark, C., Willems, A., Boucher, L., Leung, G., Kolas, N., Zhang, F., et al. (2021). The BioGRID database: A comprehensive biomedical resource of curated protein, genetic, and chemical interactions. Protein Science *30*, 187–200. 10.1002/pro.3978.

81. Ji, Z.S., Dennis Miranda, R., Newhouse, Y.M., Weisgraber, K.H., Huang, Y., and Mahley, R.W. (2002). Apolipoprotein E4 potentiates amyloid β peptide-induced lysosomal leakage and apoptosis in neuronal cells. Journal of Biological Chemistry *277*, 21821–21828. 10.1074/jbc.M112109200.

82. Harris, F.M., Brecht, W.J., Xu, Q., Mahley, R.W., and Huang, Y. (2004). Increased tau phosphorylation in apolipoprotein E4 transgenic mice is associated with activation of extracellular signal-regulated kinase. Journal of Biological Chemistry *279*, 44795–44801. 10.1074/jbc.M408127200.

83. Brecht, W.J., Harris, F.M., Chang, S., Tesseur, I., Yu, G.Q., Xu, Q., Fish, J.D., Wyss-Coray, T., Buttini, M., Mucke, L., et al. (2004). Neuron-Specific

Apolipoprotein E4 Proteolysis Is Associated with Increased Tau Phosphorylation in Brains of Transgenic Mice. Journal of Neuroscience *24*, 2527–2534. 10.1523/JNEUROSCI.4315-03.2004.

84. Piovesana, E., Magrin, C., Ente, M.S., Cantonale, O., Bellotto, M., Molinari, M., and Paganetti, P. (2023). Tau Accumulation in Degradative Organelles is Associated to Lysosomal Stress. Research Square Preprint. 10.21203/rs.3.rs-2972040/v1.

85. Rose, K., Jepson, T., Shukla, S., Maya-Romero, A., Kampmann, M., Xu, K., and Hurley, J.H. (2023). Tau fibrils induce nanoscale membrane damage and nucleate cytosolic tau at lysosomes. biorXiv Preprint. https://doi.org/10.1101/2023.08.28.555157.

86. Carosi, J.M., Hein, L.K., van den Hurk, M., Adams, R., Milky, B., Singh, S., Bardy, C., Denton, D., Kumar, S., and Sargeant, T.J. (2021). Retromer regulates the lysosomal clearance of MAPT/tau. Autophagy *17*, 2217–2237. 10.1080/15548627.2020.1821545.

87. Xu, Y., Du, S., Marsh, J.A., Horie, K., Sato, C., Ballabio, A., Karch, C.M., Holtzman, D.M., and Zheng, H. (2021). TFEB regulates lysosomal exocytosis of tau and its loss of function exacerbates tau pathology and spreading. Mol Psychiatry *26*, 5925–5939. 10.1038/s41380-020-0738-0.

88. Lee, M.J., Lee, J.H., and Rubinsztein, D.C. (2013). Tau degradation: The ubiquitin-proteasome system versus the autophagy-lysosome system. Prog Neurobiol *105*, 49–59. 10.1016/j.pneurobio.2013.03.001.

89. Hamano, T., Gendron, T.F., Causevic, E., Yen, S.H., Lin, W.L., Isidoro, C., Deture, M., and Ko, L.W. (2008). Autophagic-lysosomal perturbation enhances tau aggregation in transfectants with induced wild-type tau expression. European Journal of Neuroscience *27*, 1119–1130. 10.1111/j.1460-9568.2008.06084.x.

90. Khurana, V., Elson-Schwab, I., Fulga, T.A., Sharp, K.A., Loewen, C.A., Mulkearns, E., Tyynelä, J., Scherzer, C.R., and Feany, M.B. (2010). Lysosomal dysfunction promotes cleavage and neurotoxicity of tau in vivo. PLoS Genet *6*, 1–11. 10.1371/journal.pgen.1001026.

91. Wang, Y., Martinez-Vicente, M., Krüger, U., Kaushik, S., Wong, E., Mandelkow, E.M., Cuervo, A.M., and Mandelkow, E. (2009). Tau fragmentation, aggregation and clearance: The dual role of lysosomal processing. Hum Mol Genet *18*, 4153–4170. 10.1093/hmg/ddp367.

92. Sampognaro, P.J., Arya, S., Knudsen, G.M., Gunderson, E.L., Sandoval-Perez, A., Hodul, M., Bowles, K., Craik, C.S., Jacobson, M.P., and Kao, A.W. (2023). Mutations in α-synuclein, TDP-43 and tau prolong protein half-life through diminished degradation by lysosomal proteases. Mol Neurodegener *18*. 10.1186/s13024-023-00621-8.

93. Xiao, Q., Yan, P., Ma, X., Liu, H., Perez, R., Zhu, A., Gonzales, E., Burchett, J.M., Schuler, D.R., Cirrito, J.R., et al. (2014). Enhancing astrocytic lysosome biogenesis facilitates Aβ clearance and attenuates amyloid plaque pathogenesis. Journal of Neuroscience *34*, 9607–9620. 10.1523/JNEUROSCI.3788-13.2014.

94. Lee, J.H., Yang, D.S., Goulbourne, C.N., Im, E., Stavrides, P., Pensalfini, A., Chan, H., Bouchet-Marquis, C., Bleiwas, C., Berg, M.J., et al. (2022). Faulty

autolysosome acidification in Alzheimer's disease mouse models induces autophagic build-up of Aβ in neurons, yielding senile plaques. Nat Neurosci *25*, 688–701. 10.1038/s41593-022-01084-8.

95. Zhang, W., Xu, C., Sun, J., Shen, H.M., Wang, J., and Yang, C. (2022). Impairment of the autophagy–lysosomal pathway in Alzheimer's diseases: Pathogenic mechanisms and therapeutic potential. Acta Pharm Sin B *12*, 1019–1040. 10.1016/j.apsb.2022.01.008.

96. Mary, A., Eysert, F., Checler, F., and Chami, M. (2023). Mitophagy in Alzheimer's disease: Molecular defects and therapeutic approaches. Mol Psychiatry *28*, 202–216. 10.1038/s41380-022-01631-6.

97. Gowrishankar, S., Yuan, P., Wu, Y., Schrag, M., Paradise, S., Grutzendler, J., De Camilli, P., and Ferguson, S.M. (2015). Massive accumulation of luminal protease-deficient axonal lysosomes at Alzheimer's disease amyloid plaques. Proc Natl Acad Sci U S A *112*, E3699–E3708. 10.1073/pnas.1510329112.

98. Prasad, H., and Rao, R. (2018). Amyloid clearance defect in ApoE4 astrocytes is reversed by epigenetic correction of endosomal pH. Proc Natl Acad Sci U S A *115*, E6640–E6649. 10.1073/pnas.1801612115.

99. Andrews-Zwilling, Y., Bien-Ly, N., Xu, Q., Li, G., Bernardo, A., Yoon, S.Y., Zwilling, D., Yan, T.X., Chen, L., and Huang, Y. (2010). Apolipoprotein E4 causes age- and Tau-dependent impairment of GABAergic interneurons, leading to learning and memory deficits in mice. Journal of Neuroscience *30*, 13707–13717. 10.1523/JNEUROSCI.4040-10.2010.

100. Cummings, J., Zhou, Y., Lee, G., Zhong, K., Fonseca, J., and Cheng, F. (2023). Alzheimer's disease drug development pipeline: 2023. Alzheimer's & Dementia: Translational Research & Clinical Interventions *9*. 10.1002/trc2.12385.

101. Morrow, J.A., Hatters, D.M., Lu, B., Höchtl, P., Oberg, K.A., Rupp, B., and Weisgraber, K.H. (2002). Apolipoprotein E4 forms a molten globule: A potential basis for its association with disease. Journal of Biological Chemistry *277*, 50380–50385. 10.1074/jbc.M204898200.

102. Zellner, A., Müller, S.A., Lindner, B., Beaufort, N., Rozemuller, A.J.M., Arzberger, T., Gassen, N.C., Lichtenthaler, S.F., Kuster, B., Haffner, C., et al. (2022). Proteomic profiling in cerebral amyloid angiopathy reveals an overlap with CADASIL highlighting accumulation of HTRA1 and its substrates. Acta Neuropathol Commun *10*. 10.1186/s40478-021-01303-6.

103. Dai, J., Johnson, E.C.B., Dammer, E.B., Duong, D.M., Gearing, M., Lah, J.J., Levey, A.I., Wingo, T.S., and Seyfried, N.T. (2018). Effects of APOE Genotype on Brain Proteomic Network and Cell Type Changes in Alzheimer's Disease. Front Mol Neurosci *11*. 10.3389/fnmol.2018.00454.

104. Johnson, E.C.B., Carter, E.K., Dammer, E.B., Duong, D.M., Gerasimov, E.S., Liu, Y., Liu, J., Betarbet, R., Ping, L., Yin, L., et al. (2022). Large-scale deep multi-layer analysis of Alzheimer's disease brain reveals strong proteomic disease-related changes not observed at the RNA level. Nat Neurosci *25*, 213–225. 10.1038/s41593-021-00999-y.

105. Askenazi, M., Kavanagh, T., Pires, G., Ueberheide, B., Wisniewski, T., and Drummond, E. (2023). Compilation of reported protein changes in the brain in Alzheimer's disease. Nat Commun *14*. 10.1038/s41467-023-40208-x.

106. Aber, R., Chan, W., Mugisha, S., and Jerome-Majewska, L.A. (2019). Transmembrane emp24 domain proteins in development and disease. Genet Res (Camb). 10.1017/S0016672319000090.

107. Tian, R., Abarientos, A., Hong, J., Hashemi, S.H., Yan, R., Dräger, N., Leng, K., Nalls, M.A., Singleton, A.B., Xu, K., et al. (2021). Genome-wide CRISPRi/a screens in human neurons link lysosomal failure to ferroptosis. Nat Neurosci *24*, 1020–1034. 10.1038/s41593-021-00862-0.

108. Astillero-Lopez, V., Gonzalez-Rodriguez, M., Villar-Conde, S., Flores-Cuadrado, A., Martinez-Marcos, A., Ubeda-Banon, I., and Saiz-Sanchez, D. (2022). Neurodegeneration and astrogliosis in the entorhinal cortex in Alzheimer's disease: Stereological layer-specific assessment and proteomic analysis. Alzheimer's and Dementia *18*, 2468–2480. 10.1002/alz.12580.

109. Costa, J., Pronto-Laborinho, A., Pinto, S., Gromicho, M., Bonucci, S., Tranfield, E., Correia, C., Alexandre, B.M., and de Carvalho, M. (2020). Investigating LGALS3BP/90 K glycoprotein in the cerebrospinal fluid of patients with neurological diseases. Sci Rep *10*. 10.1038/s41598-020-62592-w.

110. Seki, T., Kanagawa, M., Kobayashi, K., Kowa, H., Yahata, N., Maruyama, K., Iwata, N., Inoue, H., and Toda, T. (2020). Galectin 3– binding protein suppresses amyloid-β production by modulating β-cleavage of amyloid precursor protein. Journal of Biological Chemistry *295*, 3678–3691. 10.1074/jbc.RA119.008703.

111. Zheng, J., Cao, Y., Yang, J., and Jiang, H. (2022). UBXD8 mediates mitochondria-associated degradation to restrain apoptosis and mitophagy. EMBO Rep *23*. 10.15252/embr.202254859.

112. Zeng, J., Shirihai, O.S., and Grinstaff, M.W. (2020). Modulating lysosomal pH: a molecular and nanoscale materials design perspective. JoLS, Journal of Life Sciences. 10.36069/jols/20201204.

113. Bouhaddou, M., Memon, D., Meyer, B., White, K.M., Rezelj, V. V., Correa Marrero, M., Polacco, B.J., Melnyk, J.E., Ulferts, S., Kaake, R.M., et al. (2020). The Global Phosphorylation Landscape of SARS-CoV-2 Infection. Cell *182*, 685-712.e19. 10.1016/j.cell.2020.06.034.

114. Li, H., Doric, Z., Berthet, A., Jorgens, D.M., Nguyen, M.K., Hsieh, I., Margulis, J., Fang, R., Debnath, J., Sesaki, H., et al. (2021). Longitudinal tracking of neuronal mitochondria delineates PINK1/Parkin-dependent mechanisms of mitochondrial recycling and degradation. Sci Adv *7*. 10.1126/sciadv.abf6580.

115. Falcón-Pérez, J.M., Nazarian, R., Sabatti, C., and Dell'Angelica, E.C. (2005). Distribution and dynamics of Lamp1-containing endocytic organelles in fibroblasts deficient in BLOC-3. J Cell Sci *118*, 5243–5255. 10.1242/jcs.02633.

116. Bindea, G., Mlecnik, B., Hackl, H., Charoentong, P., Tosolini, M., Kirilovsky, A., Fridman, W.H., Pagès, F., Trajanoski, Z., and Galon, J. (2009). ClueGO: A Cytoscape plug-in to decipher functionally grouped gene ontology and pathway annotation networks. Bioinformatics *25*, 1091–1093. 10.1093/bioinformatics/btp101.

117. Shannon, P., Markiel, A., Ozier, O., Baliga, N.S., Wang, J.T., Ramage, D., Amin, N., Schwikowski, B., and Ideker, T. (2003). Cytoscape: A software Environment for integrated models of biomolecular interaction networks. Genome Res *13*, 2498–2504. 10.1101/gr.1239303.

118. Schindelin, J., Arganda-Carreras, I., Frise, E., Kaynig, V., Longair, M., Pietzsch, T., Preibisch, S., Rueden, C., Saalfeld, S., Schmid, B., et al. (2012). Fiji: An open-source platform for biological-image analysis. Nat Methods *9*, 676–682. 10.1038/nmeth.2019.

119. Cox, J., and Mann, M. (2008). MaxQuant enables high peptide identification rates, individualized p.p.b.-range mass accuracies and proteome-wide protein quantification. Nat Biotechnol *26*, 1367–1372. 10.1038/nbt.1511.

120. Watts, J.A., Grunseich, C., Rodriguez, Y., Liu, Y., Li, D., Burdick, J.T., Bruzel, A., Crouch, R.J., Mahley, R.W., Wilson, S.H., et al. (2022). A common transcriptional mechanism involving R-loop and RNA abasic site regulates an enhancer RNA of APOE. Nucleic Acids Res *50*, 12497–12514. 10.1093/nar/gkac1107.

121. Sun, N., Yun, J., Liu, J., Malide, D., Liu, C., Rovira, I.I., Holmström, K.M., Fergusson, M.M., Yoo, Y.H., Combs, C.A., et al. (2015). Measuring In Vivo Mitophagy. Mol Cell *60*, 685–696. 10.1016/j.molcel.2015.10.009.

122. Reilly, L., Lara, E., Ramos, D., Li, Z., Pantazis, C.B., Stadler, J., Santiana, M., Roberts, J., Faghri, F., Hao, Y., et al. (2023). A fully automated FAIMS-DIA mass spectrometry-based proteomic pipeline. Cell Reports Methods, 100593. 10.1016/j.crmeth.2023.100593.

123. Olivella, R., Chiva, C., Serret, M., Mancera, D., Cozzuto, L., Hermoso, A., Borràs, E., Espadas, G., Morales, J., Pastor, O., et al. (2021). QCloud2: An Improved Cloud-based Quality-Control System for Mass-Spectrometry-based Proteomics Laboratories. J Proteome Res *20*, 2010–2013. 10.1021/acs.jproteome.0c00853.

124. Choi, M., Chang, C.Y., Clough, T., Broudy, D., Killeen, T., MacLean, B., and Vitek, O. (2014). MSstats: An R package for statistical analysis of quantitative mass spectrometry-based proteomic experiments. Bioinformatics *30*, 2524–2526. 10.1093/bioinformatics/btu305.

125. Yu, G., Wang, L.G., Han, Y., and He, Q.Y. (2012). ClusterProfiler: An R package for comparing biological themes among gene clusters. OMICS *16*, 284–287. 10.1089/omi.2011.0118.

126. Gu, Z., Eils, R., and Schlesner, M. (2016). Complex heatmaps reveal patterns and correlations in multidimensional genomic data. Bioinformatics *32*, 2847–2849. 10.1093/bioinformatics/btw313.

127. Gu, Z. (2022). Complex heatmap visualization. iMeta *1*. 10.1002/imt2.43.

128. Jurrus, E., Engel, D., Star, K., Monson, K., Brandi, J., Felberg, L.E., Brookes, D.H., Wilson, L., Chen, J., Liles, K., et al. (2018). Improvements to the APBS biomolecular solvation software suite. Protein Science *27*, 112–128. 10.1002/pro.3280.